



# Solar Tracking Strategies

---

BSc (Hons) Dissertation

L A Petrov

2010/2011

## **Abstract**

The Solar Tracking Strategies (STS) project aims to find and analyze different tracking strategies for solar energy harnessing devices. For testing purposes, a high-precision, low-cost table-top solar positioning device was designed and produced. Control over the device was achieved using a PHP server for Astronomical Algorithms (AA) computations and a Rabbit® RCM5700W microcontroller. The design of the positioning device (SPTS) was achieved using SolidWorks®. The AA testing was conducted using MATLAB® as the mathematical platform and the Horizons® [1] web-ephemeris engine served as the absolute reference. Two algorithms were chosen based on this analysis, namely the Solar Position Algorithm (SPA) [2] and Roberto Grena's ENEA [3].

The server client interactions were established and tested via an Ethernet connection between the controller and the server. The frequency of controller requests to the server was fixed to 10 interactions per second.

The Sun positioning testing procedures conducted included primary motor calibration tests and a heliostat positioning test. The measured errors from the motor positioning tests were in the range of  $0.2183^\circ$ , whereas solar positioning tests conducted showed an error of  $0.2398^\circ$ , which is largely due to the step precision of the motors.

## **Acknowledgments**

I want to express my appreciation for the generosity of Dr. Ladson Hayes. By letting me to attend the classes and laboratories for the EE32001 module and supplying me with the necessary tools, I was able to develop my understanding of programming microcontrollers and web programming.

I would like to thank Dr. Stephen Reynolds for his patience, advice and cooperation, without which this project would not progress as it did.

I would also like to thank Mr. Thomasz Kruzcek for his assistance with programming the device and Mr. William Henderson for machining the device with much care and for his advice.

## Table of Contents

Abstract .....	II
Acknowledgments .....	III
Table of Contents .....	IV
List of Figures.....	VI
List of Symbols.....	X
Glossary of Abbreviations .....	XI
1 Introduction.....	2
1.1 Solar Tracking Applications .....	2
1.2 Solar Tracking Methods.....	5
2 Theory.....	6
2.1 Solar Geometry.....	7
2.1.1 Local Hour Angle.....	7
2.1.2 Angle of Declination .....	8
2.1.3 Solar Elevation and Azimuth .....	9
2.2 Solar Tracking Precision.....	13
2.3 Solar Tracking Strategies .....	14
3 Method.....	16
3.1 Algorithm Analysis.....	16
3.1.1 Solar Position Algorithm Analysis Toolbox Development .....	17
3.1.2 Algorithm Analysis Method .....	19
3.2 Solar Positioning Testing Station Development .....	21
3.2.1 Mechanical Design.....	21
3.3 Experimental Setup .....	26
3.3.1 Hardware Test .....	26
3.3.2 Solar Tracking Tests.....	26
4 Results .....	33
4.1 Sun Position Algorithm Analysis Results .....	33
4.2 SPTS testing results .....	37
5 Discussion.....	39
5.1 Algorithm Analysis.....	39
5.2 SPTS System.....	40

5.2.1	Mechanical Design.....	40
5.2.2	Controller.....	42
5.3	Suggestions for Future Work.....	43
5.4	Suggestions for Experiments.....	43
6	Conclusions.....	45
7	Appendix A - Hardware .....	48
7.1	Controller.....	48
7.2	Display .....	49
7.3	Motors & Gearboxes .....	49
7.4	PHP Server.....	50
8	Appendix B - Software .....	51
8.1	MATLAB .....	51
8.1.1	Solar Position Algorithm Analysis Toolbox (SPAAT) .....	51
8.1.2	SPA.....	51
8.1.3	ENEA .....	52
8.1.4	JPL.....	52
8.2	Dynamic C.....	52
8.2.1	Libraries .....	52
8.2.2	Source Code.....	53
8.3	HTML and JavaScript .....	53
8.3.1	JavaScript.....	53
8.3.2	Php.....	53
9	Appendix C - Solar Position Deviations .....	54
9.1	Variation of Solar Azimuth and Elevation with deviations in declination, hour angle and latitude 54	
9.1.1	Latitude ( $\varphi$ ) .....	54
9.1.2	Declination.....	57
9.1.3	Hour Angle.....	59
9.2	Variations in Heliostat positioning estimations due to deviations in Sun Position.....	61
9.3	ENEA – JPL .....	64
9.4	SPA – JPL.....	67

## List of Figures

Figure 1 – SolFocus® CPV cells [24] .....	2
Figure 2 – Parabolic Trough CSP system (Abengoa Solar) [4] .....	3
Figure 3 – Solar Power Tower sketch [5].....	4
Figure 4 - Passive Tracking Flow Chart .....	5
Figure 5 - Active Tracking Flow Chart.....	5
Figure 6 – Earth Orbit around the Sun [7] .....	6
Figure 7 - Earth Heliocentric Radius Vector variation throughout a year .....	6
Figure 8 – Equation of Time .....	8
Figure 9 – Declination Angle variation throughout a year .....	9
Figure 10 – Solar Angles in observer plane [7].....	10
Figure 11 – Geocentric Sun Angles [7] .....	11
Figure 12 - Geocentric to Topocentric Coordinate transform [7] .....	12
Figure 13 – Heliostat Precision Requirement variation with radial distance form tower.....	13
Figure 14 - Heliostat Field Layout [8] .....	14
Figure 15 - HORIZONS WUI example settings [1] .....	18
Figure 16 – HORIZONS table settings. NOTE: Only apparent Azimuth and Elevation are ticked! [1] .....	18
Figure 17 – HORIZONS Optional settings at the table settings tab [1].....	19
Figure 18 - Algorithm analysis flow chart.....	20
Figure 19 - SPTS preliminary design .....	21
Figure 20 – SPTS secondary design .....	22
Figure 21 - SPTS after initial production.....	23
Figure 22 - SPTS with added display panel and optical encoder.....	23
Figure 23 - SPTS Display Panel Finished .....	24
Figure 24 - SPST Optical encoder mount.....	24
Figure 25 - SPTS Zenith Assembly.....	25
Figure 26 - Final SPTS device .....	25
Figure 27 - Heliostat Reference Angles [9] .....	26
Figure 28 - Heliostat vector deviation with deviation in facing angle ( $\Phi = 36.78, \lambda = 1.64$ ) .....	30
Figure 29 - Motor Precision deviation with elevation angle .....	32
Figure 30 - Deviation of ENEA zenith angle with SPA.....	33
Figure 31 - Deviation of ENEA azimuth angle with SPA azimuth .....	33

Figure 32 - ENEA sun vector deviation with SPA sun vector .....	34
Figure 33 - Mean sun vector deviation of ENEA with SPA mean sun vector for range of latitudes between -65° and 65° .....	34
Figure 34 - Max sun vector deviation of ENEA with SPA for range of latitudes.....	35
Figure 35 - Standard sun vector deviation of ENEA from SPA for range of latitudes .....	35
Figure 36 - Mean hourly sun vector deviation of ENEA from SPA .....	36
Figure 37 – RCM5700W Rabbit with the Rabbit 5000 Core .....	48
Figure 38 – Variation (relative) in solar elevation angle with deviation in Latitude. The x axis being the hour angle variation throughout a day (0° to 360°), the y-axis the declination angle variation (-24° to 24° - denoted from 0 to 48 on the graph). .....	54
Figure 39 - Variation (relative) in solar azimuth angle with deviation in latitude angle. The x-axis shows the hour angle variation throughout a day (0° to 360°). The declination angle variation (-24° to 24°) can be seen as the superimposed lines. ....	55
Figure 40 - Variation in solar azimuth angle with deviation in latitude. The x axis being the hour angle variation throughout a day (0° to 360°), the y-axis the declination angle variation (-24° to 24° - denoted from 0 to 48 on the graph).....	55
Figure 41 - Variation (relative) in solar elevation angle with deviation in latitude angle. The x-axis shows the hour angle variation throughout a day (0° to 360°). The declination angle variation (-24° to 24°) can be seen as the superimposed lines. ....	56
Figure 42 - Variation (relative) in solar elevation angle with deviation in declination angle. The x axis being the hour angle variation throughout a day (0° to 360°), the y-axis the declination angle variation (-24° to 24° - denoted from 0 to 48 on the graph). ....	57
Figure 43 - Variation (relative) in solar elevation angle with deviation in declination angle. The x-axis shows the hour angle variation throughout a day (0° to 360°). The declination angle variation (-24° to 24°) can be seen as the superimposed lines. ....	57
Figure 44 - Variation (relative) in solar azimuth angle with deviation in declination angle. The x axis being the hour angle variation throughout a day (0° to 360°), the y-axis the declination angle variation (-24° to 24° - denoted from 0 to 48 on the graph).....	58
Figure 45- Variation (relative) in solar azimuth angle with deviation in declination angle. The x-axis shows the hour angle variation throughout a day (0° to 360°). The declination angle variation (-24° to 24°) can be seen as the superimposed lines. ....	58

Figure 46 - Variation (relative) in solar azimuth angle with deviation in hour-angle. The x axis being the hour angle variation throughout a day (0° to 360°), the y-axis the declination angle variation (-24° to 24° - denoted from 0 to 48 on the graph). .....	59
Figure 47 - Variation (relative) in solar azimuth angle with deviation in hour-angle. The x-axis shows the hour angle variation throughout a day (0° to 360°). The declination angle variation (-24° to 24°) can be seen as the superimposed lines. ....	59
Figure 48 - Variation (relative) in solar elevation angle with deviation in hour-angle. The x axis being the hour angle variation throughout a day (0° to 360°), the y-axis the declination angle variation (-24° to 24° - denoted from 0 to 48 on the graph). ....	60
Figure 49 - Variation (relative) in solar elevation angle with deviation in hour-angle. The x-axis shows the hour angle variation throughout a day (0° to 360°). The declination angle variation (-24° to 24°) can be seen as the superimposed lines. ....	60
Figure 50 – Variation in heliostat azimuth positioning precision with deviation in solar azimuth angle ( $\Phi = 143.2, \lambda = 1.64$ ) .....	61
Figure 51 - Variation in heliostat azimuth positioning precision with deviation in solar azimuth angle (2D- sun elevation influence is negligible). ( $\Phi = 143.2, \lambda = 1.64$ ) .....	61
Figure 52 - Variation in heliostat azimuth positioning precision with deviation in solar elevation angle ( $\Phi = 143.2, \lambda = 1.64$ ) .....	62
Figure 53 - Variation in heliostat azimuth positioning precision with deviation in solar elevation angle (2D- sun elevation influence is negligible). ( $\Phi = 143.2, \lambda = 1.64$ ) .....	62
Figure 54 - Variation in heliostat elevation positioning precision with deviation in solar azimuth angle ( $\Phi = 143.2, \lambda = 1.64$ ) .....	63
Figure 55 - Variation in heliostat elevation positioning precision with deviation in solar elevation angle (2D- sun elevation influence is negligible). ( $\Phi = 143.2, \lambda = 1.64$ ) .....	63
Figure 56 – Deviation of ENEA zenith with JPL .....	64
Figure 57 – Azimuth deviation of ENEA from JPL .....	64
Figure 58 – Sun Vector deviation of ENEA with JPL .....	65
Figure 59 – Mean sun vector deviation of ENEA with JPL .....	65
Figure 60 – Max sun vector deviation of ENEA with JPL .....	66
Figure 61 – Standard deviation of ENEA sun vector with JPL .....	66
Figure 62 – Zenith deviation of SPA with JPL .....	67
Figure 63 - Azimuth deviation of SPA with JPL .....	67



Figure 64 – Sun vector deviation of SPA with JPL .....	68
Figure 65 – Mean sun vector deviation of SPA with JPL .....	68
Figure 66 – Max sun vector deviation of SPA with JPL.....	69
Figure 67 – Standard sun vector deviation of SPA with JPL .....	69

## List of Symbols

$A$  – Azimuth Angle

$A_H$  – Heliostat Azimuth Angle

$\alpha$  – Altitude Angle

$\alpha_H$  – Heliostat Altitude Angle

$\omega$  – Hour Angle

$\vartheta_z$  – Zenith Angle

$\delta$  – Angle of Declination

$\varphi$  – Latitude Angle

$\Phi$  – Facing Angle

$\lambda$  – Target Angle

$N$  – Day Number in a Year

$\Delta_c$  – Collector Tolerance

$\Delta_H$  - Heliostat Tolerance

$d_r$  - Radial distance of heliostat to power tower

## **Glossary of Abbreviations**

SPTS - Solar Positioning Testing Station

SPAAT – Solar Position Algorithm Analysis Toolbox

WUI - Web-User-Interface

GUI – Guided User Interface

AA - Astronomical Algorithm

SPA - Solar Position Algorithm

ENEA - Astronomical Algorithm developed by Roberto Grena at ENEA labs Italy

NREL – National Renewable Energy Laboratory (USA)

SCD - Solar Conversion Device

RTC – Real Time Clock

JPL – Jet Propulsion Laboratory

STS – Solar Tracking Strategies

CSP - Concentrated Solar Power

PV – Photovoltaic

CPV – Concentrated PV

ST – Solar Thermal

CST – Concentrated ST

PT – Parabolic Trough

SPT – Solar Power Tower

PDS – Parabolic Dish Systems

AU – Astronomical Unit

# 1 Introduction

Solar energy conversion system efficiencies have a large dependency upon the position of the given Solar Conversion Device (SCD) with respect to the solar radiant flux, where optimal theoretical results can be obtained when the device is positioned normal to the sun-vector. The heliocentric position of our planet is not constant, neither is its rotational orientation, therefore the optimal positioning for a solar energy harnessing device must be attained by a displacement mechanism. In many cases, it is preferable to install the SCD statically at the optimal tilt angle and orientation, due to increased costs and decreased reliability when dynamic positioning is involved. On the other hand, it is often the case where price and maintenance are outweighed by increased energy production per installation area or per device.

## 1.1 Solar Tracking Applications

In Concentrated Solar Power (CSP) systems, tracking the sun is essential. These systems can be of Photovoltaic (CPV) type as well as of Solar Thermal (CST) type. In the geometric domain, they can be single or two-axis tracked. The tracking precision requirement in a solar tracked system is mostly dependent upon the concentration ratio of the system.

CPV systems have a wide range of benefits over conventional PV generation. By utilizing high-efficiency multiple-junction PV cells, CPV systems can obtain efficiencies up to 40%. The concentration ratios of CPV cells range up to three orders of magnitude. This allows for expensive high-efficiency cells to be installed at a low-overall price, since most of the collector area is a reflector and the cell itself represents a miniature percentage of the device. CPV technology has also the benefit to be produced at a fast pace, since the energy and time intensive production of the semiconductor is not as relevant, because of its low material mass requirements. An example CPV is the one produced by SolFocus® showed here in Figure 1.

CST devices are the largest scale solar power plants installed so far in the world.

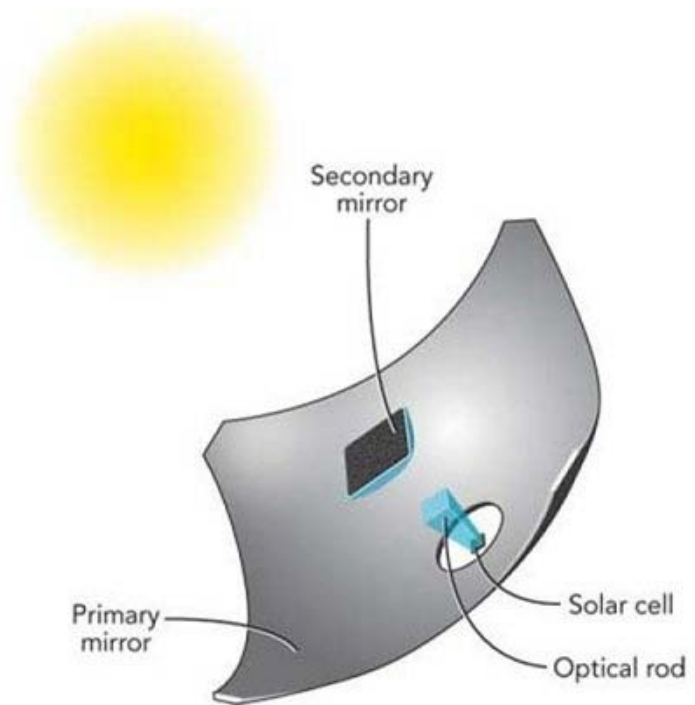
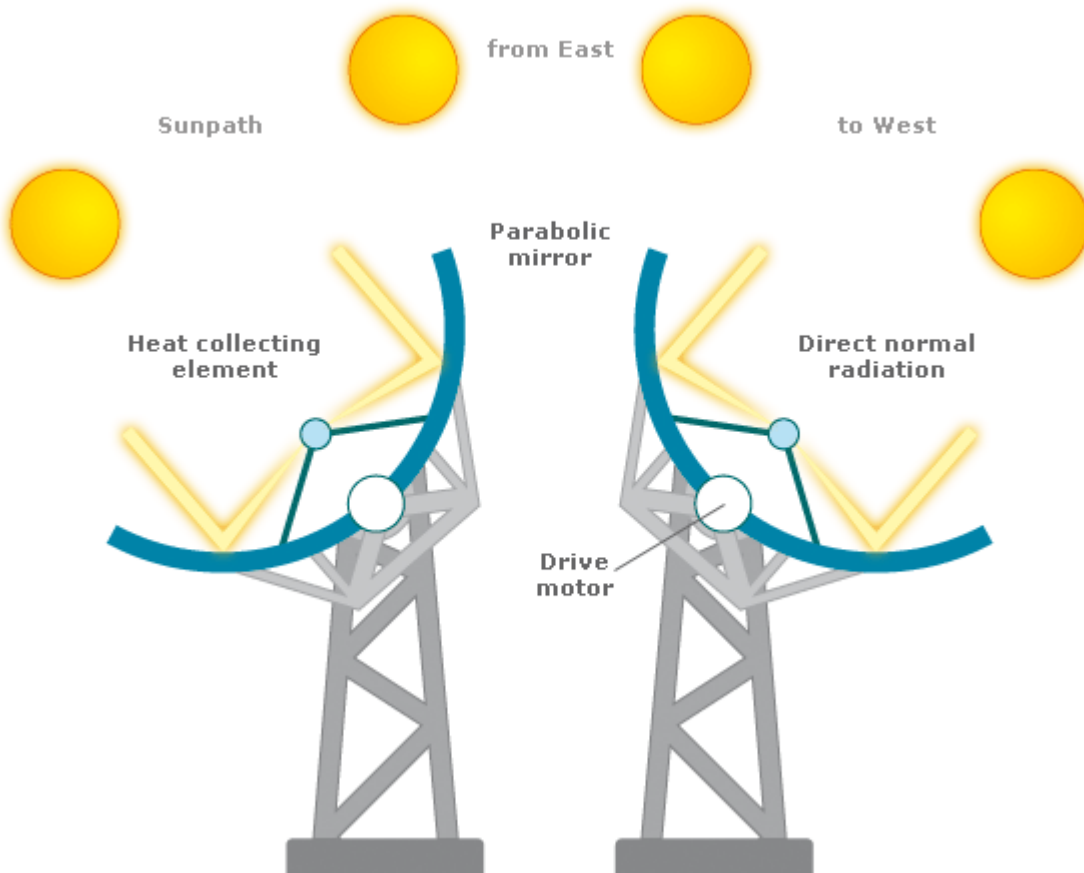


Figure 1 – SolFocus® CPV cells [24]

These devices concentrate the radiant energy coming from the sun using a variety of optical configurations. Their focal points comprise of heating elements, through which a fluid of high thermal capacity and high boiling point circulates. The fluid is channeled into a boiler to generate steam, which is used in a conventional thermal to mechanical energy conversion, such as the Rankine cycle. Some of these systems operate on a much more direct manner, by utilizing the Stirling cycle, where the hot reservoir of the engine is located at the focal point of the concentrator.

An example of a single axis tracked system is the Parabolic Trough (PT).



**Figure 2 – Parabolic Trough CSP system (Abengoa Solar) [4]**

Solar PT with thermal energy conversion is of the most proven CSP technologies and has an installed capacity of 384MW [5]. Their maximum power output of ranges from 14MW to 80MW.

Examples of a two-axis tracked system would be the Solar Power Towers (SPT), using heliostats or the Parabolic Dish Systems (PDS).

SPT comprise of an array of heliostats (movable mirrors) focused onto a tower. These systems are best suited for utility size power production from 40 to 400MWp.

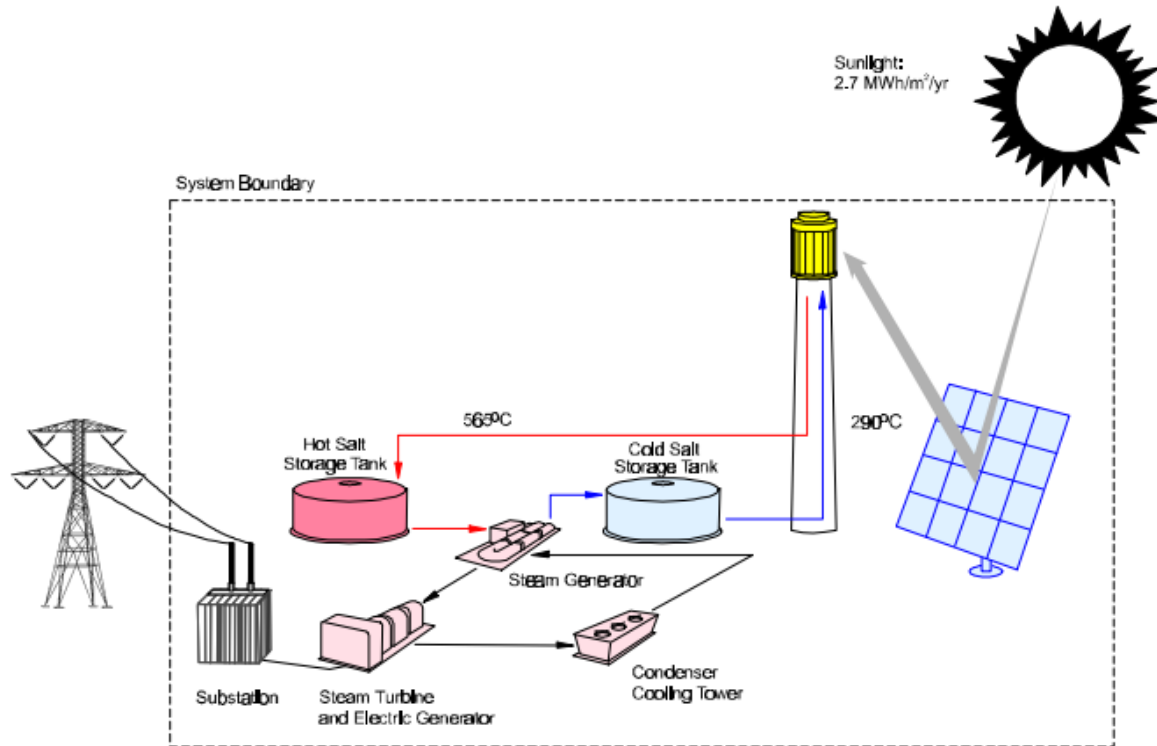


Figure 3 – Solar Power Tower sketch [5]

One and two-axis solar tracking is widely employed with conventional PV cells. The benefit of tracking the sun in terms of energy production increase can be up to 40%, depending on geographical and system conditions. This tracking is the least precision demanding due to the optical and physical specifics of the elements used. However, precise tracking is of crucial importance of the cell modeling procedures during development, since efficiency can be modeled as a function of incidence angle of the sun rays, hence a robust model of the cells can be established. This model can further be used to estimate the power output of the cells in static installations as well as in single and two-axis tracked systems with a known degree of positioning error.

## 1.2 Solar Tracking Methods

Solar tracking methods are passive, using an open-loop approach or active using a closed loop [6].

Passive tracking methods employ AA and compute the solar position as a function of topocentric position and time. This type of positioning can be more error prone if no feedback of the relative position of the tracker in each moment is provided, but is limited in precision only by the precision of the algorithms, provided that electro-mechanic precision is ideal. For this type of positioning, the azimuth axis vertical alignment and zenith horizontal alignment is of crucial importance to the overall tracking accuracy [6].

Passive tracking is the method of choice when it comes to high precision-demand solar installations, such as CPV installations.

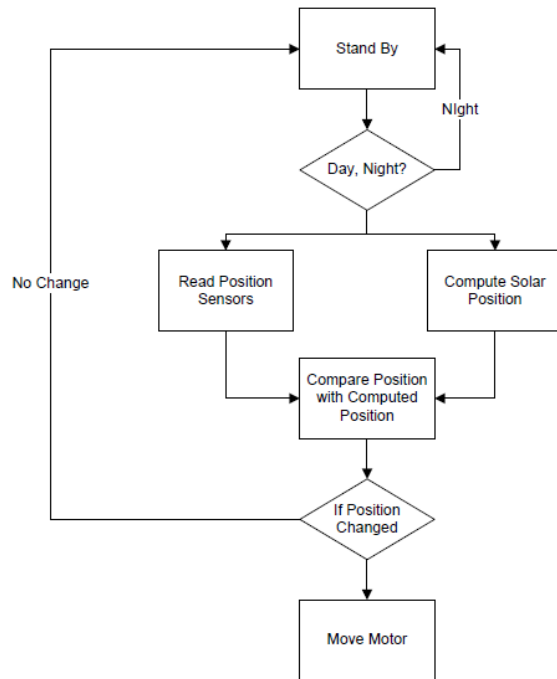


Figure 4 - Passive Tracking Flow Chart

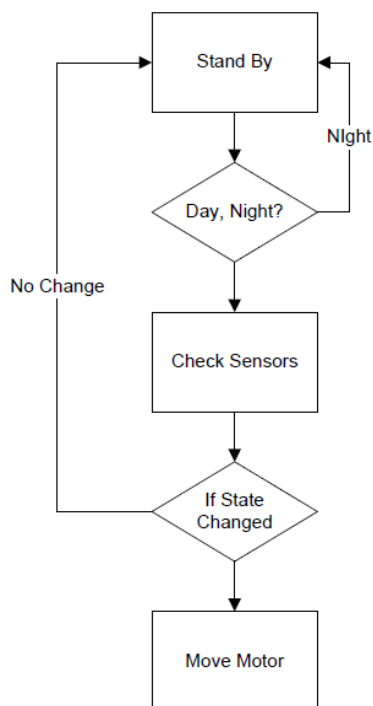


Figure 5 - Active Tracking Flow Chart

Active tracking methods use light sensitive electronics to "see" the sun and position themselves in a very dynamic fashion to the optimal position. Restrictions applying to this type of tracking are in the sensitivity of the sensors and the level of intelligence of the system. Active tracking methods work in the "brightest-point-in-the-sky" approach. Thus, unwanted movement in the "search of the sun" of the device in cloudy conditions can be expected, leading to increased power consumption, mechanical wear and decreased overall feasibility. The precision range of active tracked systems is between 0.2 to several degrees, depending on the system. Since conventional PV devices exhibit only a very small deviation in efficiency with tracking accuracy, and because active methods are of relatively low technical complexity, they are applied mainly for conventional PV tracking.

## 2 Theory

The rotation of the earth around the sun takes approximately 365.24 days. The orbit is elliptic, due to which the earth-sun distance is constantly varying. The mean center of earth – center of sun distance is equal to  $1.496 \times 10^{11} \text{m}$  or one Astronomical Unit (AU). The diurnal day-night shift that we observe is due to the earth's rotation about its polar axis and the seasonal variation is due to the declination of earth's polar axis in respect to the ecliptic plane described by the orbit around the sun.

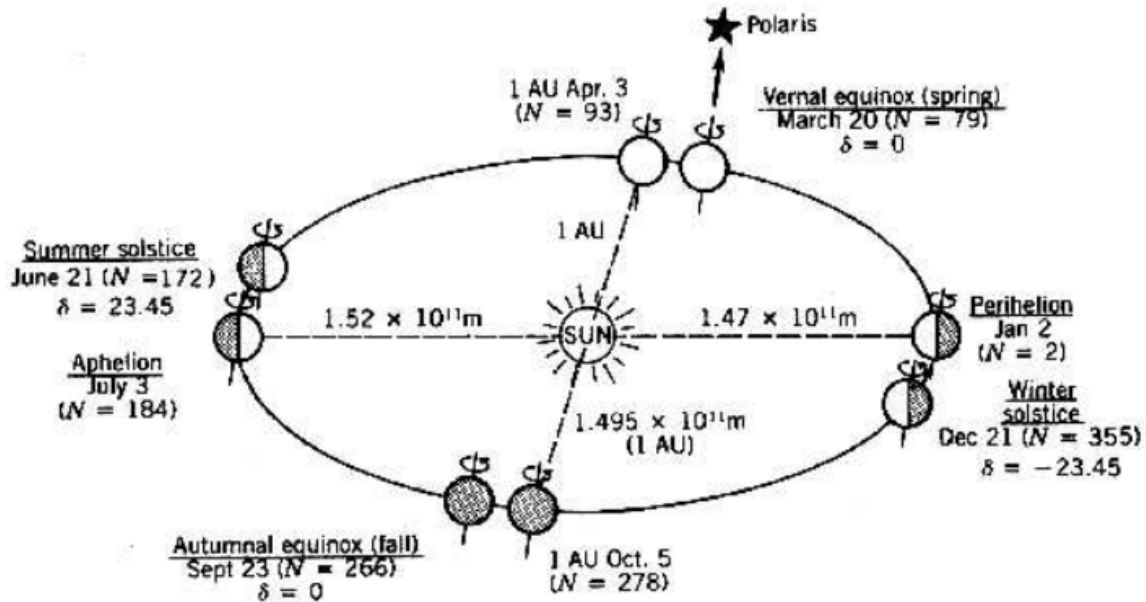


Figure 6 – Earth Orbit around the Sun [7]

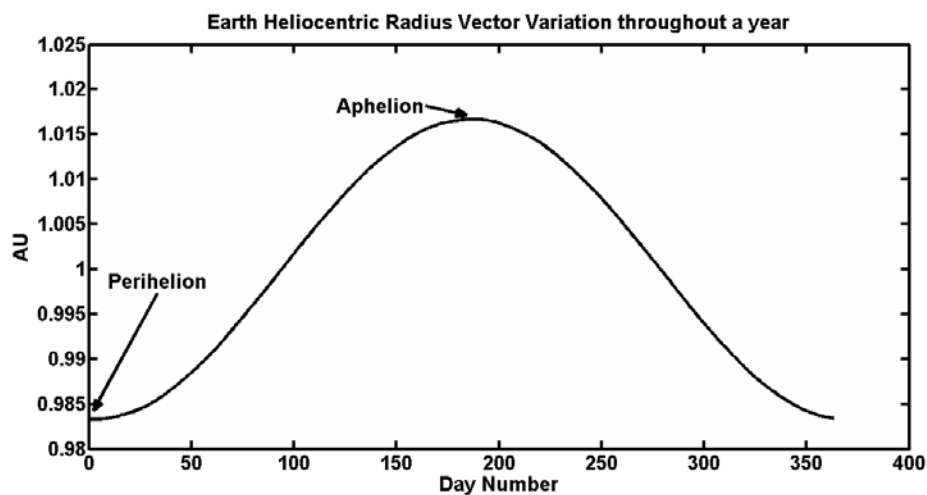


Figure 7 - Earth Heliocentric Radius Vector variation throughout a year



## 2.1 Solar Geometry

Solar position can be described in terms of its apparent Azimuth ( $A$ ) and Zenith ( $\alpha$ ) angles in respect to an observer on earth. The azimuth angle represents the angle between true North at the observer and the projection from the center of the sun disc onto the horizontal of the observer plane. The zenith angle is the complement of the solar altitude angle. Both angles may be determined as a function of Local Hour Angle ( $\omega$ ), Declination Angle ( $\delta$ ) and Latitude ( $\varphi$ ).

### 2.1.1 Local Hour Angle

The local hour angle is in a linear dependency of the local solar time  $T_s$ , which is defined as 12:00:00 at the moment during which the sun is at its highest point, at the given topocentric position. Due to the elliptic orbit of the earth, the angle of declination and the variances in the rotational frequency around its axis, the true solar time may shift by 17 minutes from the mean solar time, through the course of a year, where the mean solar time is defined as the length of an average day. The local hour angle can be expressed as

$$\omega = 15(T_s - 12) \text{ (degrees)} \quad (1)$$

The variation of true solar time can be found with the Equation of Time (EOT). Several expressions exist for determining EOT, such as the Fourier expression derived by Lamm (1981).

$$EOT = 60 \sum_{k=1}^6 \left[ A_k \cos\left(\frac{360kN}{365.25}\right) + B_k \sin\left(\frac{360kN}{365.25}\right) \right] \text{ (decimal minutes)} \quad (2)$$

$N$  is the day number in a leap year cycle (1-1461) and the constants **A** and **B** are,

k	A	B
1	2.0870E-04	0.0000E+00
2	9.2869E-03	-1.2229E-01
3	-5.2258E-02	-1.5698E-01
4	-1.3077E-03	-5.1602E-03
5	-2.1867E-03	-2.9823E-03
6	-1.5100E-04	-2.3463E-04

Table 1 – Coefficients for the Equation of time (Equation 2)

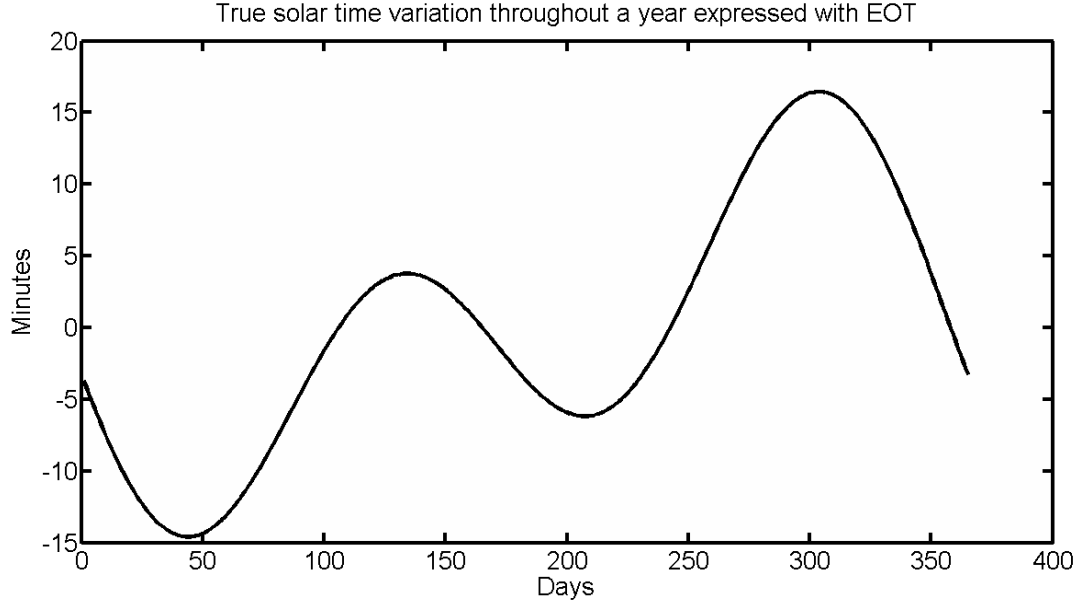


Figure 8 – Equation of Time

Conversion from local time ( $T_L$ ) to solar time

$$T_s = T_L + \frac{EOT}{60} - LC - D \text{ (decimal hours)} \quad (3)$$

$$LC = \frac{\text{Local Longitude} - \text{Longitude of Standard Meridian}}{15} \text{ (decimal hours)} \quad (4)$$

D is the daylight savings time ( $D = 1$  during summers and  $D = 0$  else).

### 2.1.2 Angle of Declination

The angle of declination is the angle the earth's polar axis makes with the ecliptic plane described by the planet's orbit. The estimation of the angle of declination can be performed through several empirical relationships with varying precision. The following Fourier expression was derived by Bourges (1985).

$$\delta = 0.372 + \sum_{k=1}^3 A_k \sin(kD) + B_k \cos(kD) \text{ (degrees)} \quad (5)$$

$$D = \frac{360}{365.25} (N - 79.346) \text{ (degrees)}$$

k	A	B
1	23.2567	-0.758
2	0.1149	0.3656
3	-0.1712	0.0201

Table 2 – Table of coefficients for Equation 5

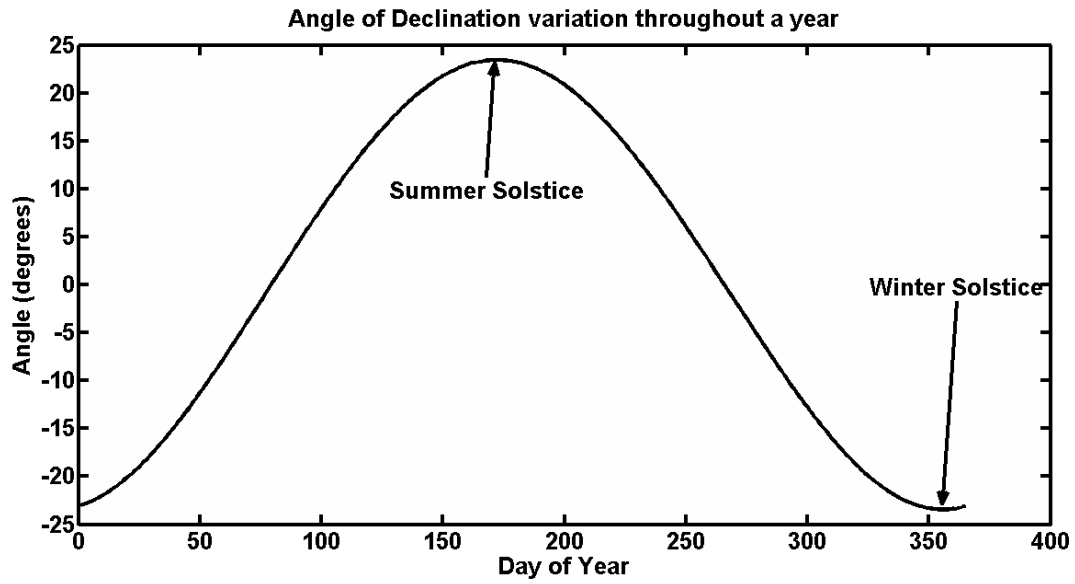


Figure 9 – Declination Angle variation throughout a year

### 2.1.3 Solar Elevation and Azimuth

The algebraic expressions for the solar elevation and azimuth angles can now be derived. The solar zenith angle is the angle the sun vector (**S**) makes with the zenith axis of the observer, as depicted in Figure 10. The zenith angle is the complementary of the solar altitude angle  $\alpha$ .

$$\vartheta_z = 90^\circ - \alpha \quad (6)$$

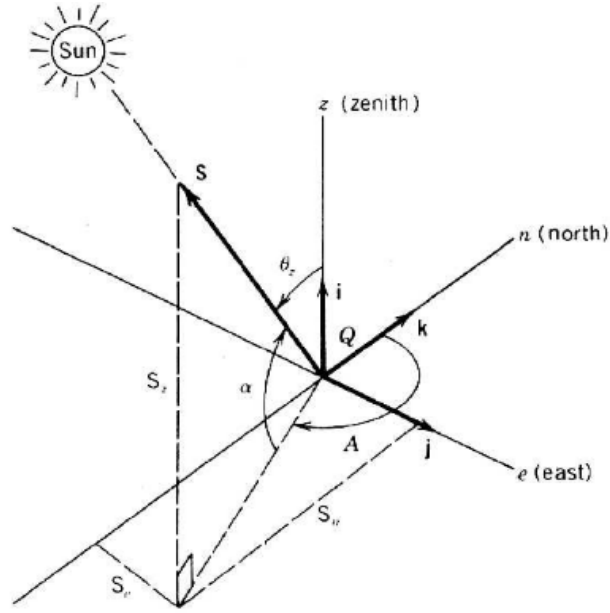


Figure 10 – Solar Angles in observer plane [7]

In vector notation,  $\mathbf{S}$  can be written as

$$\mathbf{S} = S_z \mathbf{i} + S_e \mathbf{j} + S_n \mathbf{k} \quad (7)$$

In Equation 7,  $\mathbf{i}$ ,  $\mathbf{j}$  &  $\mathbf{k}$  are the unit vectors along the Zenith ( $\mathbf{z}$ ), East ( $\mathbf{e}$ ) and North ( $\mathbf{n}$ ) axes.

In terms of solar altitude and azimuth,  $\mathbf{S}$  can be written as

$$\begin{aligned} S_z &= \sin(\alpha) \\ S_e &= \cos(\alpha) \sin(A) \\ S_n &= \cos(\alpha) \cos(A) \end{aligned} \quad (8)$$

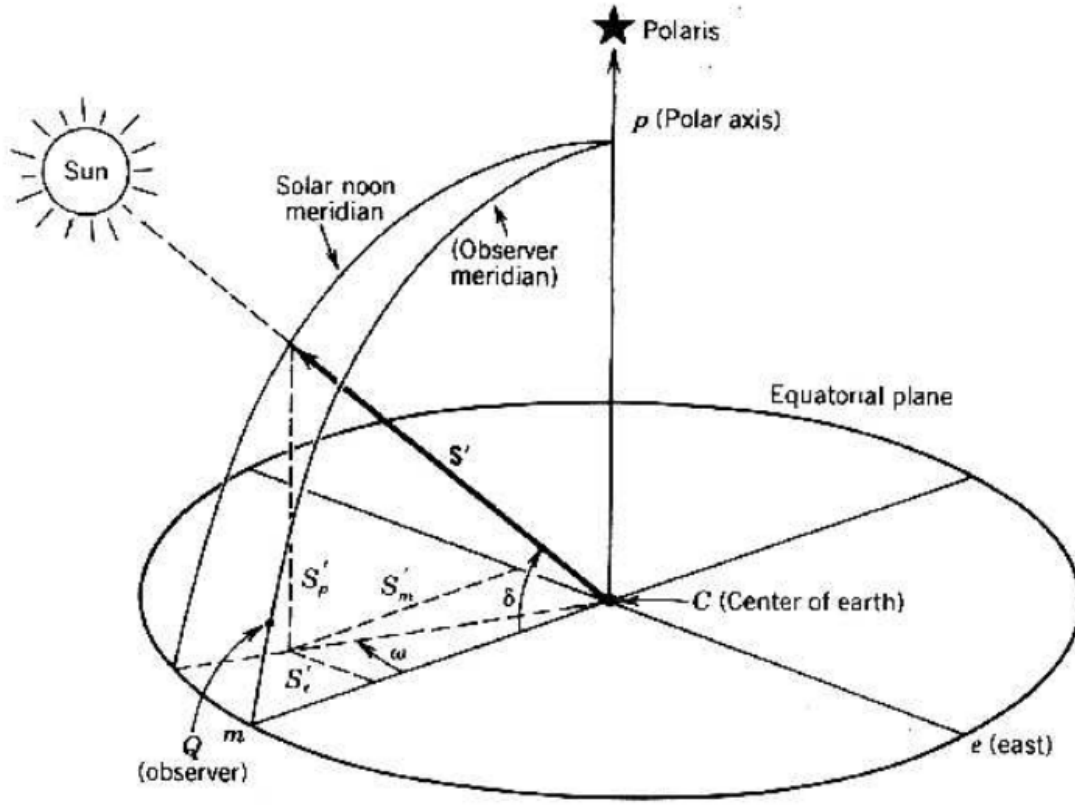


Figure 11 – Geocentric Sun Angles [7]

In the geocentric coordinate system shown in Figure 11, the  $m$  axis intersects the center of the earth and the point of intersection between the local meridian and the equatorial plane. The  $e$  axis is perpendicular to the  $m$  axis and lies also in the equatorial plane. The  $p$  axis is the normal of the equatorial plane intersecting with the North pole. The new solar vector  $S'$  may be described in terms of the solar declination and hour angles.

$$S' = S'_m i + S'_e j + S'_n k \quad (9)$$

$$\begin{aligned} S'_m &= \cos(\delta) \cos(\omega) \\ S'_e &= \cos(\delta) \sin(\omega) \\ S'_n &= \sin(\delta) \end{aligned} \quad (10)$$

The topocentric and geocentric coordinates are interrelated by a rotation about the  $e$  axis through a latitude angle ( $\varphi$ ) .

$$\begin{bmatrix} S_z \\ S_e \\ S_n \end{bmatrix} = \begin{bmatrix} \cos(\varphi) & 0 & \sin(\varphi) \\ 0 & 1 & 0 \\ -\sin(\varphi) & 0 & \cos(\varphi) \end{bmatrix} \times \begin{bmatrix} S'_m \\ S'_e \\ S'_p \end{bmatrix} \quad (11)$$

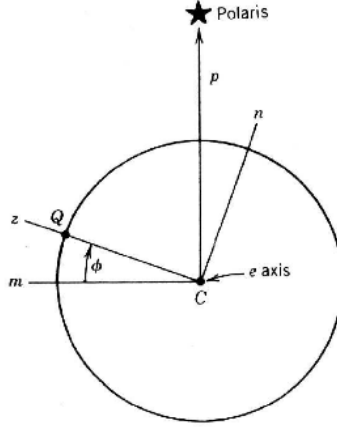


Figure 12 - Geocentric to Topocentric Coordinate transform [7]

Solving Equation 11 and substituting in Equation 8 and Equation 10 yields,

$$\begin{aligned} \sin(\alpha) &= \sin(\delta) \sin(\varphi) + \cos(\delta) \cos(\omega) \cos(\varphi) \\ \cos(\alpha) \sin(A) &= -\cos(\delta) \sin(\omega) \\ \cos(\alpha) \cos(A) &= \sin(\delta) \cos(\varphi) - \cos(\delta) \cos(\omega) \sin(\varphi) \end{aligned} \quad (12)$$

Solving Equation 12 for  $A$  and  $\alpha$ ,

$$\alpha = \arcsin(\sin(\delta) \sin(\varphi) + \cos(\delta) \cos(\omega) \cos(\varphi)) \quad (13)$$

$$A = \arctan2(\sin(\omega), \cos(\omega) \sin(\varphi) - \tan(\delta) \cos(\varphi)) \quad (14)$$

## 2.2 Solar Tracking Precision

Passive solar tracking employs solar position algorithms, such as the ones described in the equations derived above, based on declination angle and equation of time estimations. Depending on the precision requirement of the given solar application, the amount of computations within the algorithms varies several magnitudes.

As was mentioned in the introduction, the precision requirement for the given solar application is roughly dependent upon the concentration ratio of the optical aperture. For example, when a SPT is taken into consideration, the heliostat tolerance  $\Delta_H$  is dependent upon the tolerance of the collector aperture  $\Delta_C$  and the distance between the heliostat and the collector. By Pythagoras, the dependency of heliostat positioning precision with radial distance ( $d_r$ ) from the power tower can be written as,

$$\Delta_H(d_r, \Delta_C) = \text{atan} \left( \frac{\Delta_C}{\sqrt{(h_T - h_h)^2 + d_r^2}} \right) \quad (15)$$

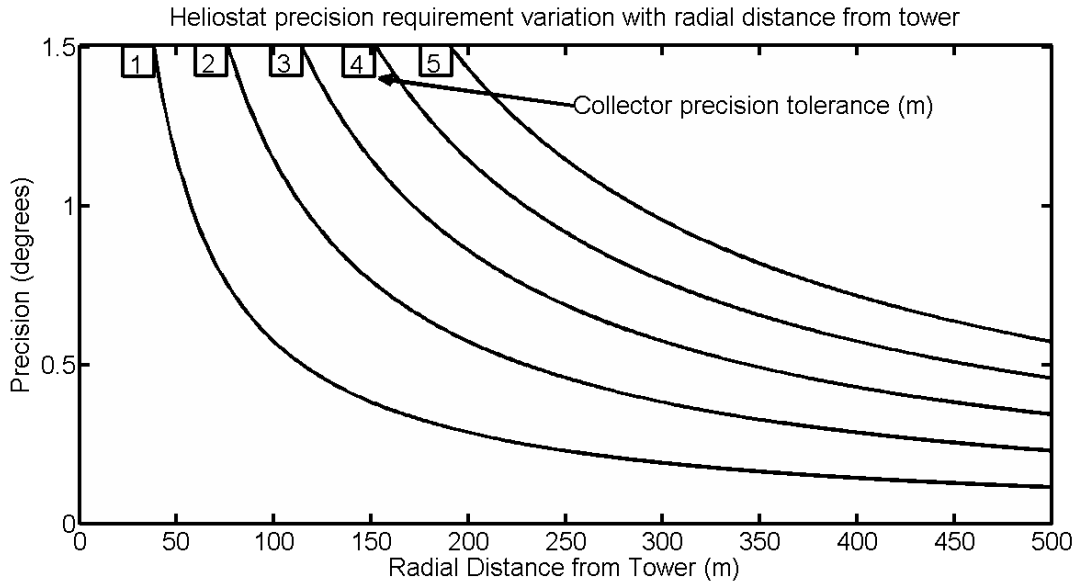


Figure 13 – Heliostat Precision Requirement variation with radial distance form tower

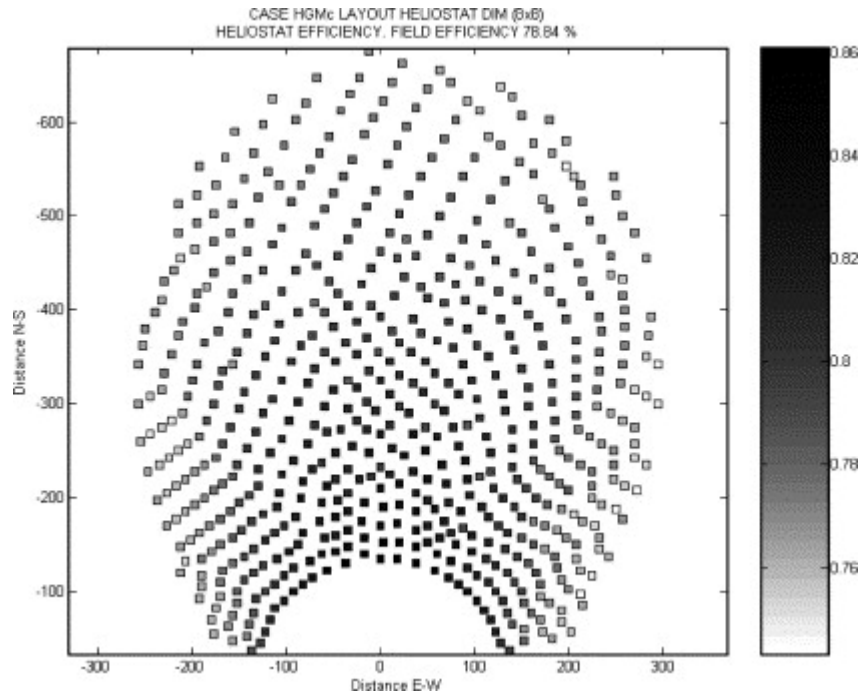


Figure 14 - Heliostat Field Layout [8]

As can be seen from Figure 14, the radial distance from a heliostat to the tower can be close to 1 kilometer. This will translate into a heliostat precision limitation of  $0.057^\circ$  if the receiver tolerance is one meter.

## 2.3 Solar Tracking Strategies

The heliostat example aimed to illustrate the importance tracking precision plays in CSP type of systems with a large concentration ratio. Two main factors are governing the precision of a passively controlled device:

1. Tracking Method
  - a. Active
  - b. Passive
  - c. Hybrid
2. Hardware
  - a. Electro-Mechanics
  - b. Controller

Electro-mechanics are in an intimate relationship with the feasibility of a given solar tracking device, due to which they need to be considered once the decision upon the tracking strategy has been made. The



controller has a lesser impact, but its influence onto final device precision and price can be significant. For example, using an expensive desktop computer for controlling a solar tracker of several PV modules is of no physical or economical sense, since the PC alone might consume more energy than the system produces and may cost more. In the other extreme, if a Dish-Stirling system is to be controlled by a series of light dependent resistors connected through some logic circuits, the economic gains in the controller will be of no significance, compared to the losses the system might have. Thus, a balanced choice of electro-mechanics and control methods are crucial for tracking system effectiveness.

The choice of a tracking method is the beginning of every solar tracking development process. The decision, whether passive or active method should be used, or whether a simpler or a computationally intensive algorithm should be used, can be made based on knowledge of system precision requirements. In other words, the two main factors influencing the entire decision process for design and application of a solar tracker are the system precision requirement and the precision limitations of the tracking method into consideration.

The present thesis is entirely focused on finding the precision limitations of different tracking methods. For this, an experimental apparatus was developed, consisting of an advanced solar tracking device and algorithm analysis software.

### **3 Method**

For solar tracking strategies analysis, the need of an advanced solar tracking device arose. This device had to be robust, economical, easily producible and more than anything, adaptable.

The requirement for robustness was justified by the fact that the system had to be able to withstand mechanical wear and loads. It had to be built, so that it was easy to assemble/disassemble, calibrate and put to work.

The system had to be economical due to the financial restrictions upon the project. In fact, economic constraints played a vital role in system evolution, as they do in any development process. For example, the initial plan for the SPTS device to use  $0.9^\circ$  step bi-polar stepper motors combined with harmonic drive gearboxes. The superiority of this motor-gearbox pair is very well demonstrated by their price, which was around ten times more expensive, than the elements that were used in the final assembly.

Ease of production was aimed throughout all the SPTS design stages. The final assembly was to be consisting of easy to manufacture geometric shapes, such as plates, pillars and cylindrical axes.

The adaptivity of a solar tracking testing apparatus is essential. This type of system needs to be able to work with different astronomic algorithms, with different logic algorithms (when active tracking is concerned) and different motor control techniques. The system might also be required estimate different algorithms and/or tracking techniques simultaneously and to log data.

The solution was found in a microcontroller - web-server configuration. In this type of system, the controller can be programmed with general hardware control code, whereas specific tracking methods, comprising of large and computationally intensive astronomical, general mathematical and logic control algorithms, can be implemented onto the web server. As a benefit from this choice, the ability to interact with the device from distance (through the internet) was made possible as well as several other benefits were found, to be discussed later on in this paper.

#### **3.1 Algorithm Analysis**

The final aim of this system was to be able to work under a set of conditions so as to generate data for the precision of one or the other solar tracking strategy chosen. However, to be able to estimate the preciseness of a given positioning technique, detailed knowledge of the precision of the given algorithm was needed.

Solar position algorithms are numerical regression models of ephemeris data. They compute the local hour and declination angles, based on which, through Equation 13 and Equation 14 the solar position is determined at the given topocentric position. The precision of the algorithms varies by several magnitudes, as does their computational intensity.

### 3.1.1 Solar Position Algorithm Analysis Toolbox Development

In order to approve the validity of precision of a certain algorithm, an algorithm analysis toolbox in the MATLAB® environment was developed, as part of this project. The toolbox consists of reference ephemeris data that, as of knowledge to the author, is the limit in precision in solar position data available in the world, as of time of writing.

The data was generated at the online ephemeris engine -HORIZONS [1], developed by the Jet Propulsion Laboratory (JPL) at the California Institute of Technology (Caltech), USA. The interactive web-user interface of HORIZONS allows fast ephemeris data generation with a large amount of options.

The following steps demonstrate the settings of HORIZONS when the ephemeris data used in this work was generated:

1. Set the Ephemeris Type to: **Observer**;
2. Set the Target Body to: **Sun [Sol][10]**;
3. Set the Observer Location to: **user defined ( 0°00'00.0"E, 40°00'00.0"N, 0.5 km )**;
  - a. Longitude = 0.00 °;
  - b. Latitude = 40.00° (this value was varied between -65° and 65° in steps of 5°);
  - c. Elevation above sea level = 0.5km;
4. Set the Time Span to: **Start=2010-01-01, Stop=2020-01-01, Step=1 h**;
5. Set the Table Settings to: **QUANTITIES=4; date/time format=JD; time digits=FRACSEC; angle format=DEG**;
6. Set the Display Output to: **download/save (plain text file)**;

Figures 15, 16 and 17 illustrate the settings for the web-ephemeris engine. Please note, that while within the Table Settings:

1. Apparent Elevation and Azimuth are the only value of interest (Figure 16);
2. Julian Day is the preferred time format (Figure 17);
3. Decimal degrees is the preferred angular format (Figure 17);

4. The airless model was chosen, as different refraction corrections can influence the apparent position data, which is the reason for the analysis (Figure 17);

The time span was chosen to be a decade, as there was a limitation upon the file size that could be generated. Files were generated for 8 decades (2010 to 2080) for 27 latitudes (-65° to 65°), thus making 216 text files, each of size 3.43MB, consisting of close to 90k lines of text. These files were read, filtered and converted into .mat files in MATLAB, for ease of integration with .m codes. After the conversion, the total file size for the 8 decade hourly ephemeris data-set was 316MB.

**Current Settings**

Ephemeris Type [\[change\]](#) : **OBSERVER**  
 Target Body [\[change\]](#) : **Sun [Sol]** [10]  
 Observer Location [\[change\]](#) : user defined ( 0°00'00.0"E, 40°00'00.0"N, 0.5 km )  
 Time Span [\[change\]](#) : Start=2010-01-01, Stop=2020-01-01, Step=1 h  
 Table Settings [\[change\]](#) : QUANTITIES=4; date/time format=JD; time digits=FRACSEC; angle format=DEG  
 Display/Output [\[change\]](#) : **download/save** (plain text file)

Figure 15 - HORIZONS WUI example settings [1]

1. <input type="checkbox"/> Astrometric RA & DEC * 2. <input type="checkbox"/> Apparent RA & DEC 3. <input type="checkbox"/> Rates; RA & DEC * 4. <input checked="" type="checkbox"/> Apparent AZ & EL 5. <input type="checkbox"/> Rates; AZ & EL 6. <input type="checkbox"/> Sat. X & Y, pos. ang 7. <input type="checkbox"/> Local app. sid. time 8. <input type="checkbox"/> Airmass 9. <input type="checkbox"/> Vis mag. & Surf Brt 10. <input type="checkbox"/> Illuminated fraction 11. <input type="checkbox"/> Defect of illumin. 12. <input type="checkbox"/> Sat. angle separ/vis 13. <input type="checkbox"/> Target angular diam. 14. <input type="checkbox"/> Obs sub-lng & sub-lat	15. <input type="checkbox"/> Sun sub-long & sub-lat 16. <input type="checkbox"/> Sub Sun Pos. Ang & Dis 17. <input type="checkbox"/> N. Pole Pos. Ang & Dis 18. <input type="checkbox"/> Helio eclip. lon & lat 19. <input type="checkbox"/> Helio range & rng rate 20. <input type="checkbox"/> Obsrv range & rng rate 21. <input type="checkbox"/> One-Way Light-Time 22. <input type="checkbox"/> Speed wrt Sun & obsrvr 23. <input type="checkbox"/> Sun-Obsrvr-Target angl 24. <input type="checkbox"/> Sun-Target-Obsrvr angl 25. <input type="checkbox"/> Targ-Obsrv-Moon/Illum% 26. <input type="checkbox"/> Obsr-Primary-Targ angl 27. <input type="checkbox"/> Pos. Ang;radius & -vel 28. <input type="checkbox"/> Orbit plane angle	29. <input type="checkbox"/> Constellation ID 30. <input type="checkbox"/> Delta-T (CT - UT) * 31. <input type="checkbox"/> Obs eclip. lon & lat 32. <input type="checkbox"/> North pole RA & DEC 33. <input type="checkbox"/> Galactic latitude 34. <input type="checkbox"/> Local app. SOLAR time 35. <input type="checkbox"/> Earth->Site lt-time > 36. <input type="checkbox"/> RA & DEC uncertainty > 37. <input type="checkbox"/> POS error ellipse > 38. <input type="checkbox"/> POS uncertainty (RSS) > 39. <input type="checkbox"/> Range & Rng-rate sig. > 40. <input type="checkbox"/> Doppler/delay sigmas
---	---	--

Figure 16 – HORIZONS table settings. NOTE: Only apparent Azimuth and Elevation are ticked! [1]

**Optional observer-table settings:**

date/time format :	Julian Day	-- display date/time in year-month-day and/or Julian-day format
time digits :	fractional seconds (HH:MM:SS.SSS)	-- controls output precision of time
angle format :	decimal degrees	-- select RA/Dec output format
output units :	km & km/s	-- units for most output quantities
range units :	Astronomical Units	-- units for range-type quantities
refraction model :	airless model (no refraction)	-- select atmospheric refraction model
airmass limit :		-- suppress output when airmass is greater than this limit
elevation cutoff :		(deg) -- suppress output when object elevation is less than this limit
solar elong. limits :	0 - 180	(deg) -- suppress output when solar elongation is outside this range
suppress range-rate :	<input type="checkbox"/>	-- suppress range-rate for range/range-rate output
skip daylight :	<input type="checkbox"/>	-- suppress output during daylight
extra precision :	<input type="checkbox"/>	-- output addition digits for RA/Dec quantities
RTS flag :	disable	-- output data only at target rise/transit/set (RTS)
reference system :	ICRF/J2000.0	-- reference frame for geometric and astrometric quantities
CSV format :	<input type="checkbox"/>	-- output data in Comma-Separated-Variables (CSV) format
object page :	<input checked="" type="checkbox"/>	-- include object information/data page on output

**Figure 17 – HORIZONS Optional settings at the table settings tab [1]**

Having precise ephemeris reference data enables algorithms to be analyzed in respect to it. Several solar position algorithms were written for the algorithm analysis toolbox and can be accessed within it, however only two were thoroughly analyzed, namely SPA and ENEA. The reason for this choice is time limitations for the project.

Description of how to use the toolbox can be found in Appendix B – Software -> SPAAT.

### 3.1.2 Algorithm Analysis Method

The algorithm analysis code was written to be able interpolate between the discrete data points in the spatial and temporal domains. However, since inaccuracies were observed when interpolation was performed, the algorithm analysis was conducted only with the exact data points from the ephemeris files. The flow chart in Figure 18 illustrates the method of error matrix generation.

As was mentioned above, all algorithm comparisons were done with no atmospheric correction procedures. In this way, only the numerical procedures for hour and declination angle were essentially compared.

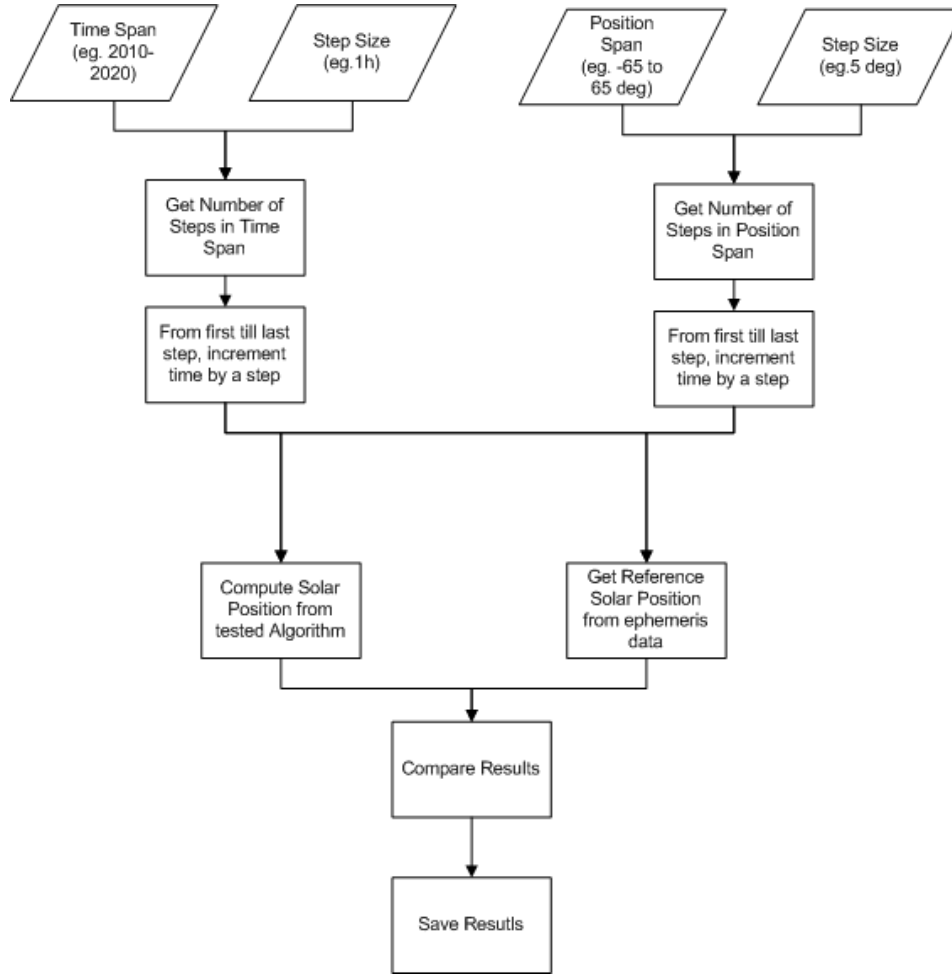


Figure 18 - Algorithm analysis flow chart

For the results comparison, the generated errors in elevation (complement of zenith) and azimuth were converted into a sun vector error  $\Delta_{sv}$ , by

$$\Delta_{sv} = \sqrt{\Delta_{\alpha}^2 + (\Delta_A \cos(\alpha))^2} \quad (16)$$

It needs to be mentioned, that the error matrix generation is an immense amount of computations. In example, the computation of the SPA algorithm for one year at one latitude, takes approximately 25 minutes on a quad-core PC. The code for the error analysis was run at the University of Dundee Advanced Computer Engineering Laboratory (ACE LAB) on several machines in one day, in order to estimate the error matrices.

## 3.2 Solar Positioning Testing Station Development

### 3.2.1 Mechanical Design

SPTS design followed an inference path, where the mechanical assembly could be envisaged only if details of certain components were known. Initially, due to the variability in the decisions upon the individual components, such as motors and gearboxes, rotary encoders and power supply, the mechanical design of SPTS was envisaged as depicted in the following figure.

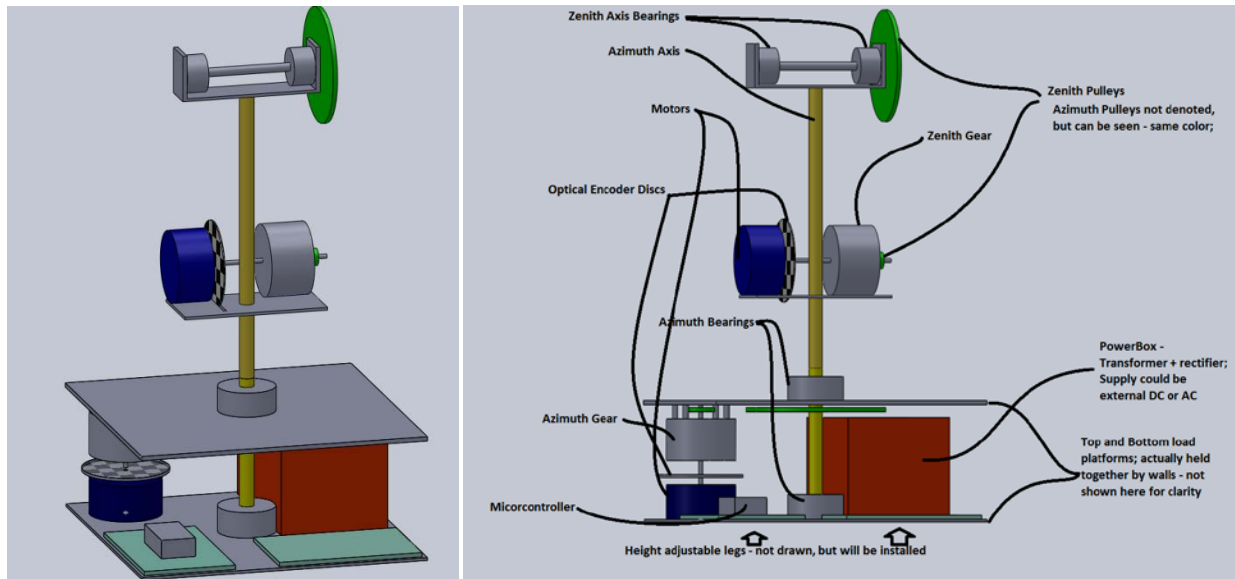
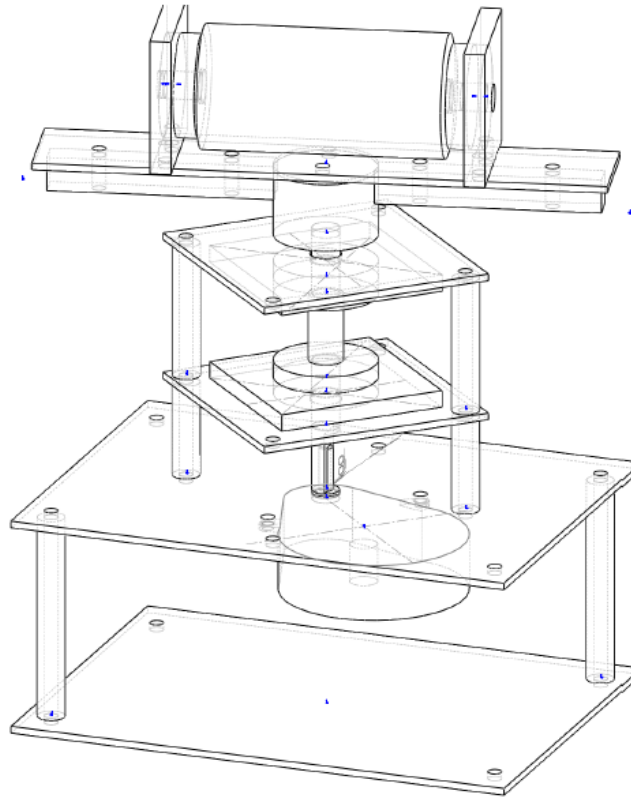


Figure 19 - SPTS preliminary design

Although very immature, this design turned out to be accurate to a large degree with the final assembly of the project. The main features included and decisions that were made here are:

1. Zenith and Azimuth Motors RS332953 – these motors were supplied initially, but were substituted by the smaller models of the same manufacturer, namely RS332947;
2. Rotary Encoders – Initially, rotary optical encoders were envisaged for the system;
3. Gearboxes – Harmonic Drive gearboxes were planned, but were substituted by the RS motor-gearbox sets with the RS332947 motors;
4. Azimuth axis, Elevation axis and Base Assembly – The general idea for zenith and azimuth was kept, although the drive transmission was of a different character. The Base Assembly was intended to be large enough so as to be able to house the necessary electronics and electro-mechanics within it, and this option was successfully kept;
5. Bearings – All bearings were dismissed without precision compromise. This led to great simplification in the production stage;

As a product of prolonged negotiations regarding mechanical details, electronics and electro-mechanics to be bought for this project, the system evolved through several steps, as depicted by the following set of figures.



**Figure 20 – SPTS secondary design**

The design decisions made to produce the Figure 20 – SPTS secondary design drawing, were based on the obtained RS332947 Motor – Gearbox pairs. Having the precise dimensions of the motors and gearboxes allowed for detailed drawings to be produced.



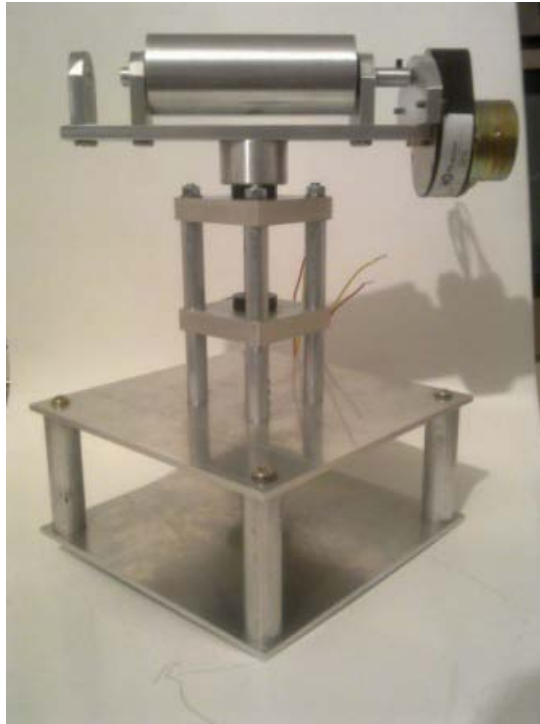


**Figure 21 - SPTS after initial production**

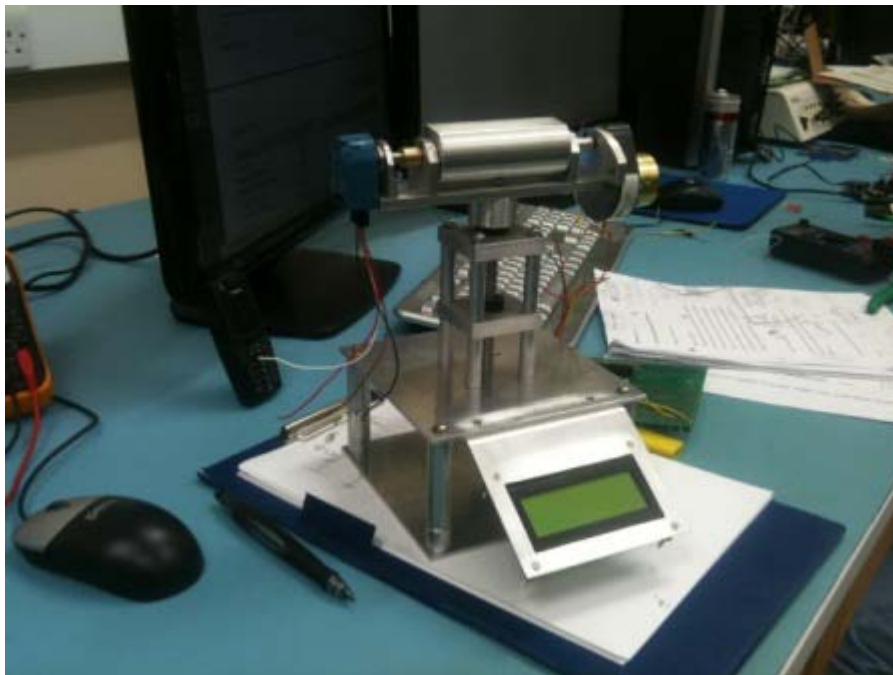


**Figure 22 - SPTS with added display panel and optical encoder**



Figure 23 - SPTS Display Panel Finished

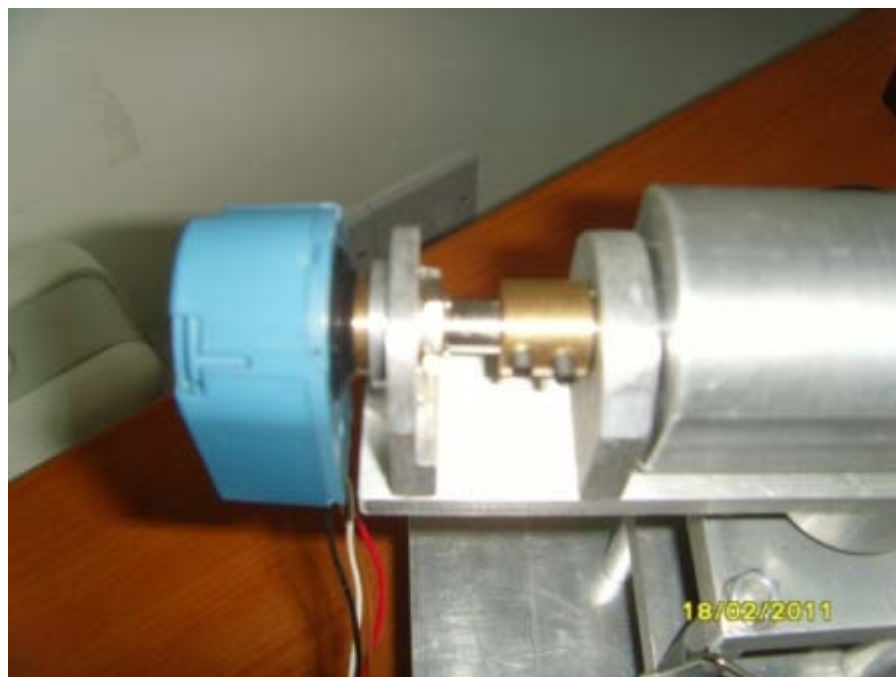


Figure 24 - SPST Optical encoder mount



Figure 25 - SPTS Zenith Assembly



Figure 26 - Final SPTS device

### 3.3 Experimental Setup

#### 3.3.1 Hardware Test

The SPTS device was calibrated through a low-power laser device mounted onto its zenith axis. The laser played the role of an extension of the zenith axis, thus every small increment in azimuth or zenith could be detected, if a measurement of the laser-spot deviation from a surface several meters away from the device was taken. This allowed for the motor code to be developed fast and the backlashes that were present in the gearboxes could be corrected.

In the motor calibration and testing, the system was pointing at a white-board, a known distance away from the device. On the white-board a mesh of pre-defined dots was drawn. SPTS was then programmed to follow the dots in repetitive manner, starting from an initial position and ending at the same initial position. A measurement of the deviation from every dot, in every cycle was taken, as well as a measurement of the deviation of the pointing accuracy at the initial spot.

#### 3.3.2 Solar Tracking Tests

In order to test the positioning precision of SPTS in respect to the sun vector, a heliostat setup was chosen. The experiment consisted of setting up SPTS to a reference point onto a target of known coordinates and knowing the coordinates of the device, and the solar position allowed for programming the device to track the sun in such a way, so the reflection of the mirror was always centered at the reference point onto the target.

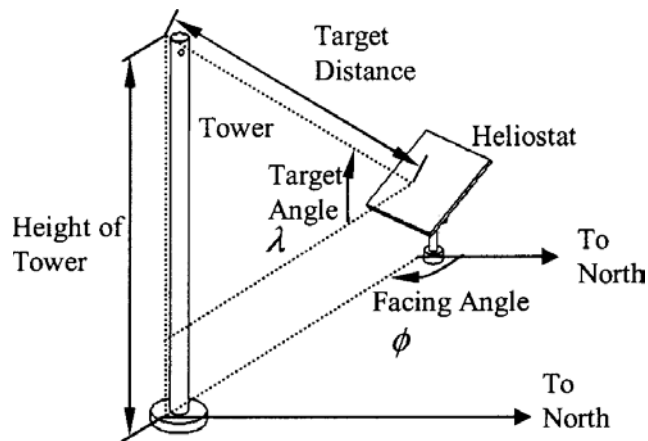


Figure 27 - Heliostat Reference Angles [9]

Figure 27 illustrates the naming conventions for the heliostat reference angles. The important angles are the facing angle ( $\Phi$ ) and the target angle( $\lambda$ ).

The reference angles of the system in respect to the heliostat can be found by knowing the corresponding coordinates of both. These were found through the Google Earth® software, since a precise surveying could not be done. By knowing the latitudes and longitudes with their respective variances, one can establish the facing angle of the system.

$$\bar{\Phi} = 2\pi + \text{atan}\left(\frac{\Delta_{Lat}}{\Delta_{Lon}}\right) \quad (17)$$

$$\Delta_{Lat} = Lat_{Target} - Lat_{SPTS}$$

$$\Delta_{Lon} = Lon_{Target} - Lon_{SPTS}$$

The latitude and longitude were taken for the system and target to be

$Lat_{Target}$	56.45748°
$Lat_{SPTS}$	56.45756°
$\Delta_{Lat}$	<b>-0.00008°</b>
$Lon_{Target}$	-2.980034°
$Lon_{SPTS}$	-2.980141°
$\Delta_{Lon}$	<b>0.000107°</b>

**Table 3**

The variance of measurements of the latitude and longitudes was assumed to be

$$\sigma = \sigma_{Lon} = \sigma_{Lat} = 0.000015^\circ$$

Because both latitude and both longitude measurements might contribute to the error

$$\sigma_{\Delta_{Lon}} = \sigma_{\Delta_{Lat}} = \sqrt{2\sigma^2} = 0.000021^\circ$$

The facing angle can be expressed with its variance to be

$$\Phi = \bar{\Phi} \pm \delta\Phi$$

where

$$\delta\Phi = \sqrt{\left(\frac{\partial\Phi}{\partial\Delta_{Lat}}\sigma_{\Delta_{Lat}}\right)^2 + \left(\frac{\partial\Phi}{\partial\Delta_{Lon}}\sigma_{\Delta_{Lon}}\right)^2} \quad (18)$$

$$\frac{\partial\Phi}{\partial\Delta_{Lat}} = \frac{1}{\Delta_{Lon}\left(\frac{\Delta_{Lat}^2}{\Delta_{Lon}^2} + 1\right)}, \text{ and } \frac{\partial\Phi}{\partial\Delta_{Lon}} = -\frac{\Delta_{Lat}}{\Delta_{Lon}^2\left(\frac{\Delta_{Lat}^2}{\Delta_{Lon}^2} + 1\right)} \quad (19)$$

Substituting in, one gets

$$\Phi = 143.2159 \pm 0.1123^\circ$$

The target angle is dependent on the difference of the height ( $\Delta_h$ ) of the apparatus in respect to the height of the target and to the radial distance from the target ( $d_r$ ), which were measured to be 0.3m and 10.5m respectively.

$$\bar{\lambda} = \text{atan}\left(\frac{\Delta_h}{d_r}\right) = \text{atan}\left(\frac{0.30m}{10.5m}\right) = 1.6366^\circ \quad (20)$$

Following the same mechanics of computations as for the facing angle, the deviation of the target angle, assuming the deviation in radial distance ( $\sigma_{\Delta_{dr}}$ ) and height difference ( $\sigma_{\Delta_h}$ ) are 0.5m and 0.1m respectively, can be estimated to be

$$\delta\lambda = \sqrt{\left(-\frac{\Delta_h}{d_r^2\left(\frac{\Delta_h^2}{d_r^2} + 1\right)}\sigma_{\Delta_{dr}}\right)^2 + \left(\frac{1}{d_r\left(\frac{\Delta_h^2}{d_r^2} + 1\right)}\sigma_{\Delta_h}\right)^2} = 0.0096^\circ \quad (21)$$

Thus,

$$\lambda = 1.6366 \pm 0.0096^\circ$$

The error in the latitude estimation contributes also to an error in zenith and azimuth angles estimation. When solving Equation 13 and 14 for deviation with latitude angle, one arrives at the following equations

$$\delta\alpha = \frac{\partial\alpha}{\partial\varphi}\delta\varphi = \left( \frac{\cos(\varphi)\sin(\delta) - \cos(\omega)\cos(\delta)\sin(\varphi)}{\sqrt{1 - (\sin(\delta)\sin(\varphi) + \cos(\omega)\cos(\delta)\cos(\varphi))^2}} \right) \delta\varphi \quad (22)$$

$$\delta A = \frac{\partial A}{\partial\varphi}\delta\varphi = - \left( \frac{\sin(\omega)(\tan(\delta)\sin(\varphi) + \cos(\varphi)\cos(\omega))}{\cos(\omega)\tan(\delta) - \cos(\omega)\sin(\varphi)^2 \left( \frac{\sin(\omega)^2}{\cos(\varphi)\tan(\delta) - \cos(\omega)\sin(\varphi)^2} + 1 \right)} \right) \delta\varphi \quad (23)$$

Substituting in the numbers for  $\omega$ ,  $\delta$  and  $\varphi$  for the approximate times when the experiment was conducted, the deviation of elevation and azimuth angle with deviation in latitude can be established. This deviation is plotted in surface plots in Appendix C.

The approximate values of deviation for solar azimuth and elevation as of time of the experiment are  $-8.85E - 8^\circ$  and  $1.98E - 5^\circ$  respectively. The solar azimuth and elevation angles influence the heliostat angles as

$$\delta A_H = \frac{\partial A_H}{\partial A}\delta A + \frac{\partial A_H}{\partial\alpha}\delta\alpha \quad \text{and} \quad \delta\alpha_H = \frac{\partial\alpha_H}{\partial A}\delta A + \frac{\partial\alpha_H}{\partial\alpha}\delta\alpha \quad (24)$$

The solutions to these equations were found using the MATLAB® symbolic math toolbox. They will not be displayed in this thesis, as this is out of scope of the work being conducted. However, the exact analytical solutions can be found in the source-codes section of the Project Disc.

This mathematical exercise is performed in order to establish the precision limitation induced by inexact knowledge of latitude and longitude of the device and target. The final value of interest is the variation in the heliostat precision

$$\Delta_H = \sqrt{\delta\alpha_H^2 + (\delta A_H \cos(\alpha_H))^2 + \left( \frac{\partial\Delta_H}{\partial\Phi}\delta\Phi \right)^2 + \left( \frac{\partial\Delta_H}{\partial\lambda}\delta\lambda \right)^2} \quad (25)$$

Where, the heliostat elevation and azimuth angles are given by

$$\alpha_H = \text{asin} \left( \frac{\sin(\alpha) - \sin(\lambda)}{2 \cos(\vartheta)} \right) \quad (26)$$

$$A_H = \pi - \text{asin}\left(\frac{\cos(\lambda) \sin(\Phi) + \cos(\alpha) \sin(A)}{2 \cos(\alpha) \cos(\alpha_H)}\right) \quad (27)$$

The angle  $\vartheta$  is the incidence angle of the solar vector onto the heliostat.

$$\vartheta = \frac{1}{2} \text{acos}(-\sin(\lambda) \sin(\alpha) + \cos(\lambda) \sin(\Phi) \cos(\alpha) \sin(A) + \cos(\lambda) \cos(\Phi) \cos(\alpha) \cos(A)) \quad (28)$$

The values found for  $\delta A_H$ ,  $\delta \alpha_H$ ,  $\left(\frac{\partial \Delta_H}{\partial \Phi}\right)$  and  $\left(\frac{\partial \Delta_H}{\partial \lambda}\right)$  for the range of time of the experiments conducted are  $-2.3857E - 5^\circ$ ,  $2.0011E - 5^\circ$ ,  $\sim 0.27$  and  $0.47$  respectively (see Figure 28). Since the values of solar position deviation are two magnitudes lower, than the precision of the algorithm used (ENEA), the precision of the algorithm itself can be used for the heliostat vector precision limitation calculation. Thus, the expected deviation for the heliostat reflection, due to inaccurate knowledge of latitude, longitude and height difference from the target can be calculated to be

$$\Delta_H \cong \sqrt{0.003^2 + ((-0.270) * 0.1123^\circ)^2 + (0.47 * 0.0096^\circ)^2} \cong 0.0308^\circ$$

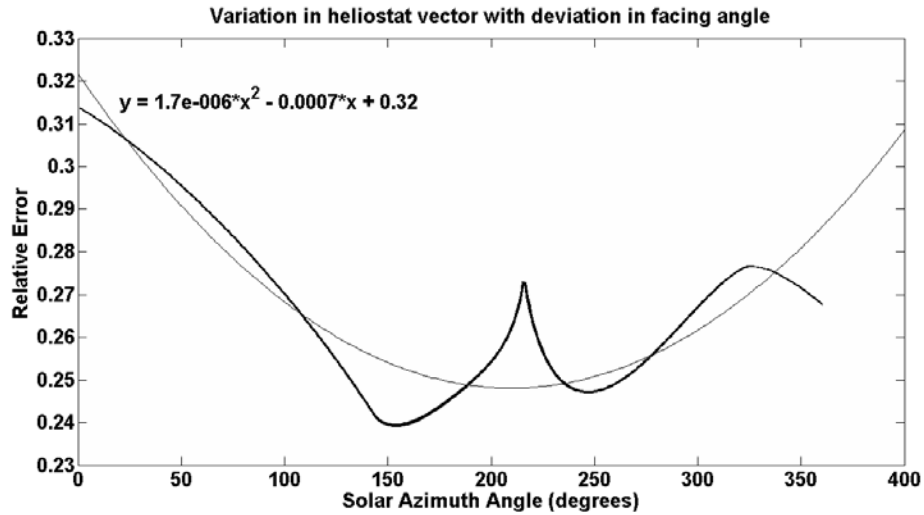


Figure 28 - Heliostat vector deviation with deviation in facing angle ( $\Phi = 36.78$ ,  $\lambda = 1.64$ )



Having the system set-up at known coordinates to reflect the solar image onto a distant target of also known coordinates, the system can be directed towards the center of the sun disc. The solar positioning precision can be calculated as follows

$$\Delta_{Sun} = \sqrt{\Delta_H^2 + \Delta_{SPTS}^2 + \Delta_{Motor}^2} \quad (29)$$

The precision of system positioning is fundamentally limited by the resolution of the motors and the ability of the system to move from one point in 3d space to the next.

$$\Delta_{Motor} = \sqrt{\left(\frac{Step_{\alpha}}{2}\right)^2 + \left(\frac{Step_{Tol,\alpha}}{2}\right)^2 + \left(\frac{\cos(\alpha) Step_A}{2}\right)^2 + \left(\frac{\cos(\alpha) Step_{Tol,A}}{2}\right)^2} \quad (30)$$

The 0.5 factor is included in Equation 30 since the system positions itself towards certain values by rounding up the steps. Thus, a value for azimuth of  $0.091^\circ$  would correspond to two steps, when in full step mode of operation, and the system would position itself at  $0.12^\circ$ , which is closer to the desired value, instead of staying at  $0.06^\circ$  until  $0.12^\circ$  is reached.

Since every variable for the motor positioning precision calculation can be found in the motor's datasheet, taking an average value for the elevation angle of  $30^\circ$ , the motor precision can be calculated.

$$\Delta_{Motor (FS)} = \sqrt{\left(\frac{\cos(30^\circ)0.06}{2}\right)^2 + \left(\frac{0.15}{2}\right)^2 + \left(\frac{\cos(30^\circ)0.667}{125}\right)^2 + \left(\frac{0.667}{50}\right)^2} = 0.0820^\circ$$

The factors 125 and 50 correspond to the azimuth and zenith gearbox ratios. If the motor is setup however in the half-step mode, then the step precision of zenith and azimuth would be doubled, and the total system motor precision would be

$$\Delta_{Motor (HS)} = \sqrt{\left(\frac{\cos(30^\circ)0.03}{2}\right)^2 + \left(\frac{0.075}{2}\right)^2 + \left(\frac{\cos(30^\circ)0.667}{125}\right)^2 + \left(\frac{0.667}{50}\right)^2} = 0.0421^\circ$$

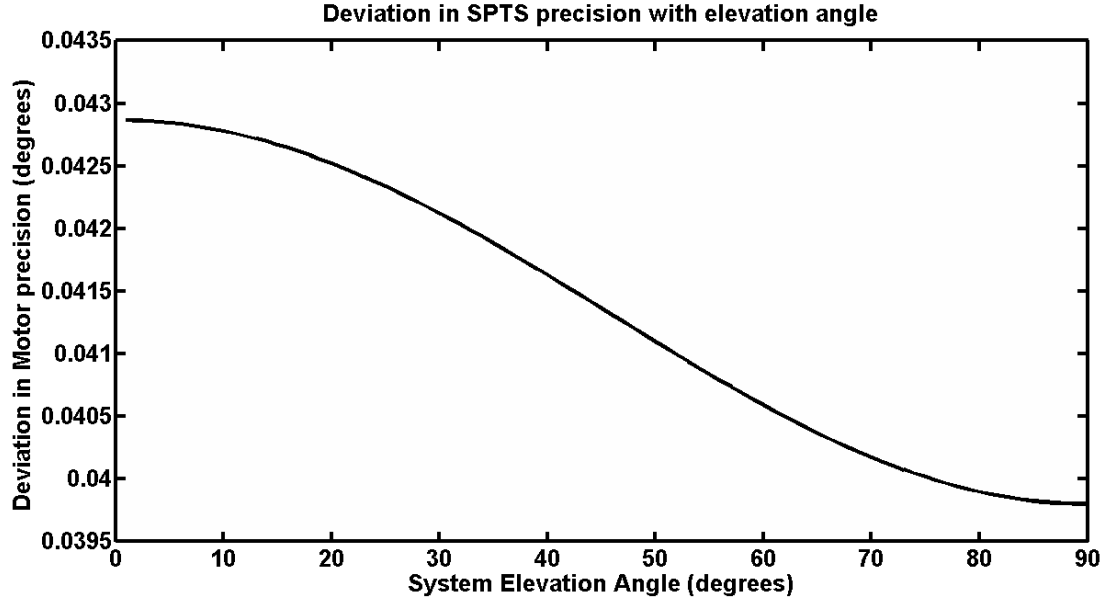


Figure 29 - Motor Precision deviation with elevation angle

As can be seen from Figure 29, the motor precision does not vary significantly with elevation angle. The derived value of 0.0421° degrees will be used throughout this thesis, as at approximately such elevation angles was the system testing conducted at most times.

Finally, the system positioning precision can be derived by knowing the random positioning error, which was measured to be  $\sqrt{\Delta_{SPTS}^2} \cong 0.2183^\circ$ . Thus, the sun-positioning ability of the system is limited to a precision of approximately

$$\Delta_{Sun} \approx \sqrt{0.0308^2 + 0.0421^2 + 0.2183^2} \approx 0.2244^\circ$$

## 4 Results

### 4.1 Sun Position Algorithm Analysis Results

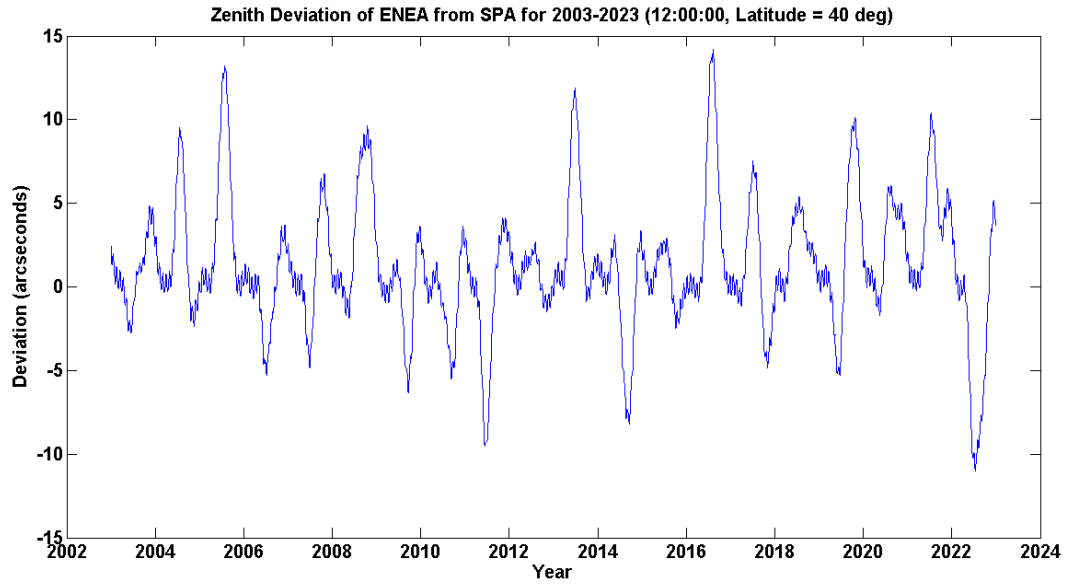


Figure 30 - Deviation of ENEA zenith angle with SPA

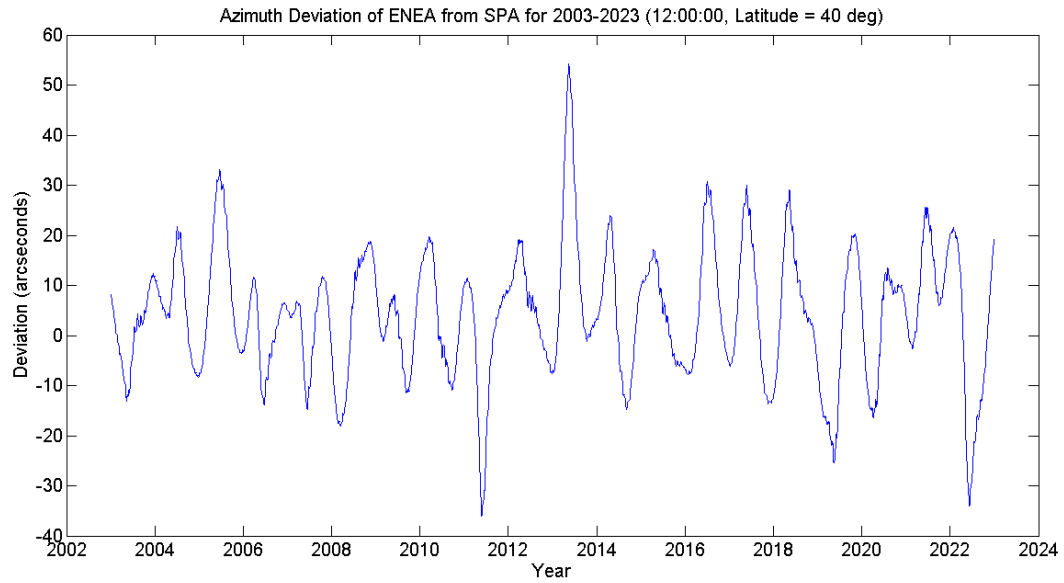


Figure 31 - Deviation of ENEA azimuth angle with SPA azimuth

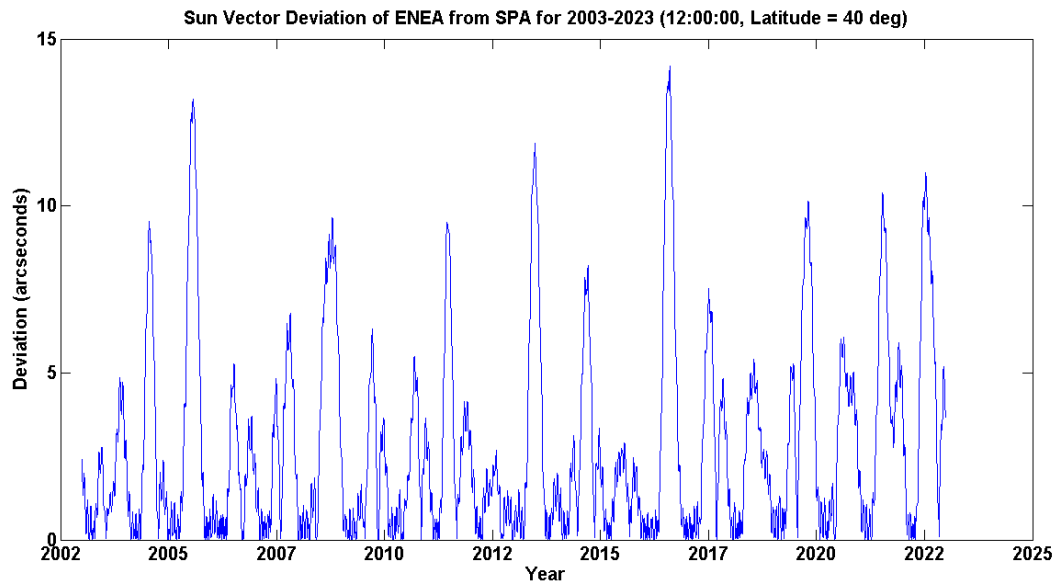


Figure 32 - ENEA sun vector deviation with SPA sun vector

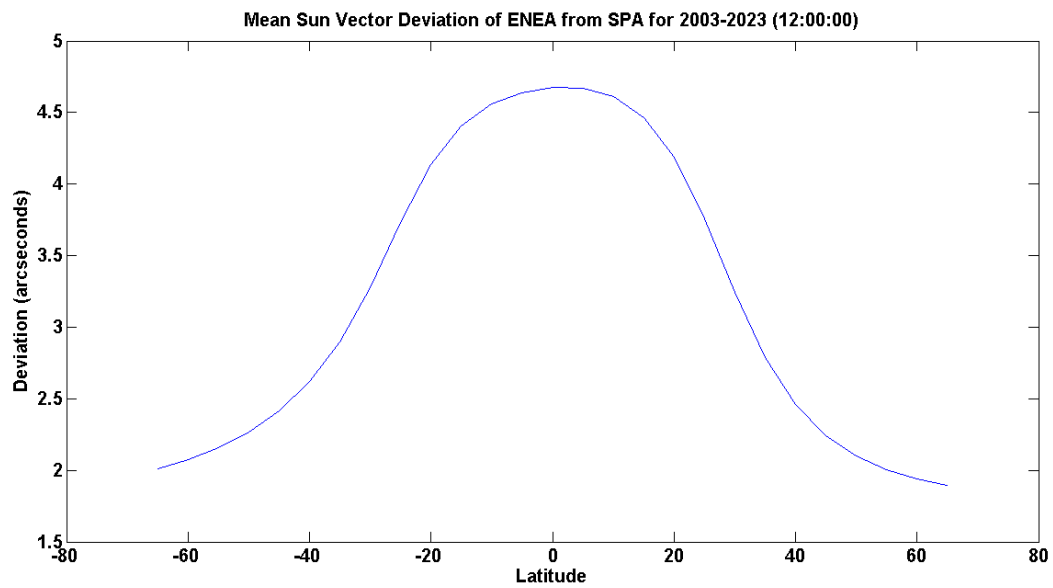


Figure 33 - Mean sun vector deviation of ENEA with SPA mean sun vector for range of latitudes between  $-65^{\circ}$  and  $65^{\circ}$

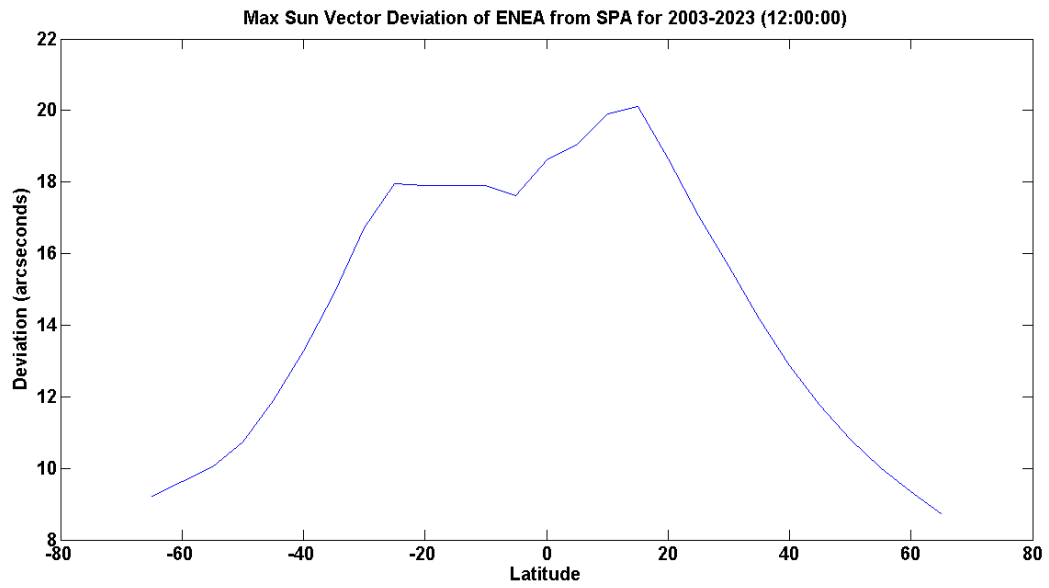


Figure 34 - Max sun vector deviation of ENEA with SPA for range of latitudes

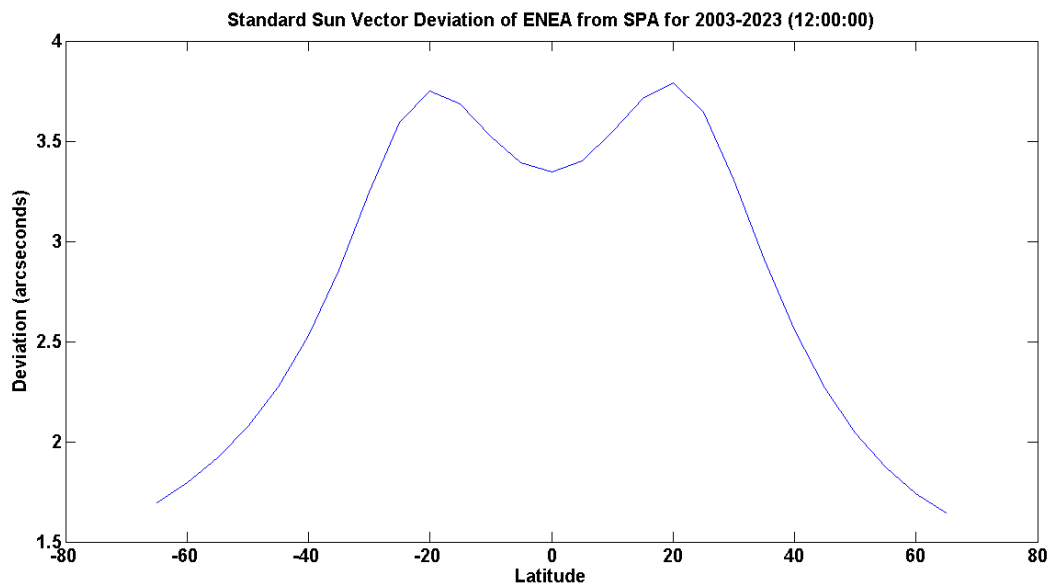


Figure 35 - Standard sun vector deviation of ENEA from SPA for range of latitudes

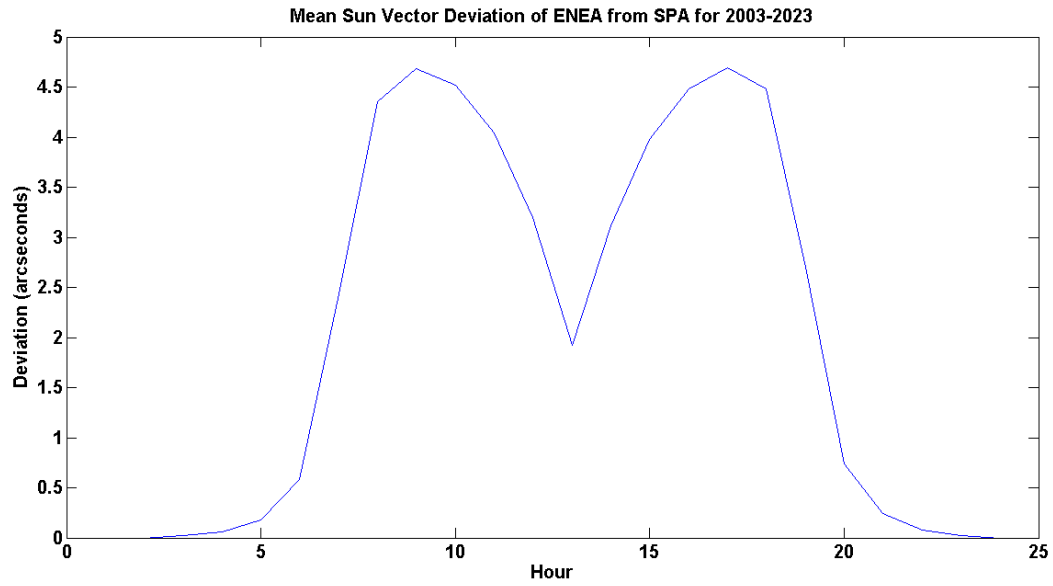


Figure 36 - Mean hourly sun vector deviation of ENEA from SPA

Algorithm Tested for 12:00:00	Mean Error (arc second)	Standard Deviation (arc second)	Max Error (arc second)
ENEA – SPA (2003-2023)	<b>2.1052</b> (5.8478E-4°)	<b>1.9847</b> (5.5131E-4°)	<b>10.7875</b> (0.0030°)
ENEA – JPL (2010-2020)	<b>3.5575</b> (9.8819E-4°)	<b>3.1105</b> (8.6403E-4°)	<b>23.9699</b> (0.0067°)
SPA – JPL (2010-2020)	<b>2.3064</b> (6.4067E-4°)	<b>1.9361</b> (5.3781E-4°)	<b>7.0806</b> (0.0020°)

Table 4 – Algorithm Analysis Results

## 4.2 SPTS testing results

The initial system positioning testing was done by letting the system move from an initial (0,0) point through an arbitrary point and back to the initial position. The mean zenith position deviation measured was  $\overline{\Delta_z} = 0.0410$ , whereas the mean azimuth position deviation was  $\overline{\Delta_A} = 0.1637$ , hence the mean system positioning precision may be calculated as

$$\Delta_{SPTS,Init} = \sqrt{\overline{\Delta_{zenit\ h}}^2 + \overline{\Delta_{azimut\ h}}^2} = 0.1688^\circ$$

The second test was conducted by letting the system go through all the steps and return to the initial position. The max radial deviation from the initial point measured after a series of repetitions was 4cm which accounts for

$$\Delta_{SPTS,Max} = \text{atan}\left(\frac{0.04}{10.5}\right) = 0.2183^\circ$$

When the system is in operation it may repeatedly go from heliostat tracking to sun tracking, thus the maximum error can be assumed for total system precision.

$$\Delta_{SPTS} = \Delta_{SPTS,Max}$$

The final system tests were conducted however with the zenith motor operating in half-step mode and the azimuth motor in full-step mode for reasons to be discussed in this work. The theoretical motor precision can be said to be

$$\Delta_{Motor\ (FS/HS)} = \sqrt{\left(\frac{\cos(30)0.06}{2}\right)^2 + \left(\frac{0.075}{2}\right)^2 + \left(\frac{\cos(30)0.667}{125}\right)^2 + \left(\frac{0.667}{50}\right)^2} = 0.0946^\circ$$

Thus maximum sun positioning error is,

$$\Delta_{Sun} = \sqrt{0.0305^2 + 0.0946^2 + 0.2183^2} = 0.2398^\circ$$

Another test was conducted by setting up the system in heliostat mode by adjusting the reflection of the sun onto the target. Then, the system was positioned towards the sun and back to the target. The deviation of the reflection with the target, after a set of tests, was measured to be  $\Delta_H = 0.1719^\circ$ .

The final test conducted is letting the system operate in Heliostat mode for a long period of time. System operation was recorded for periods of several minutes up to 1.5 hrs. The maximum deviation measured

for such periods was initially above  $0.5^\circ$ . After several bug fixes in the program operating the motors and positioning them in space, the precision decreased to  $0.3^\circ$ . The following set of images depicts the device in operation for around 2 minutes.

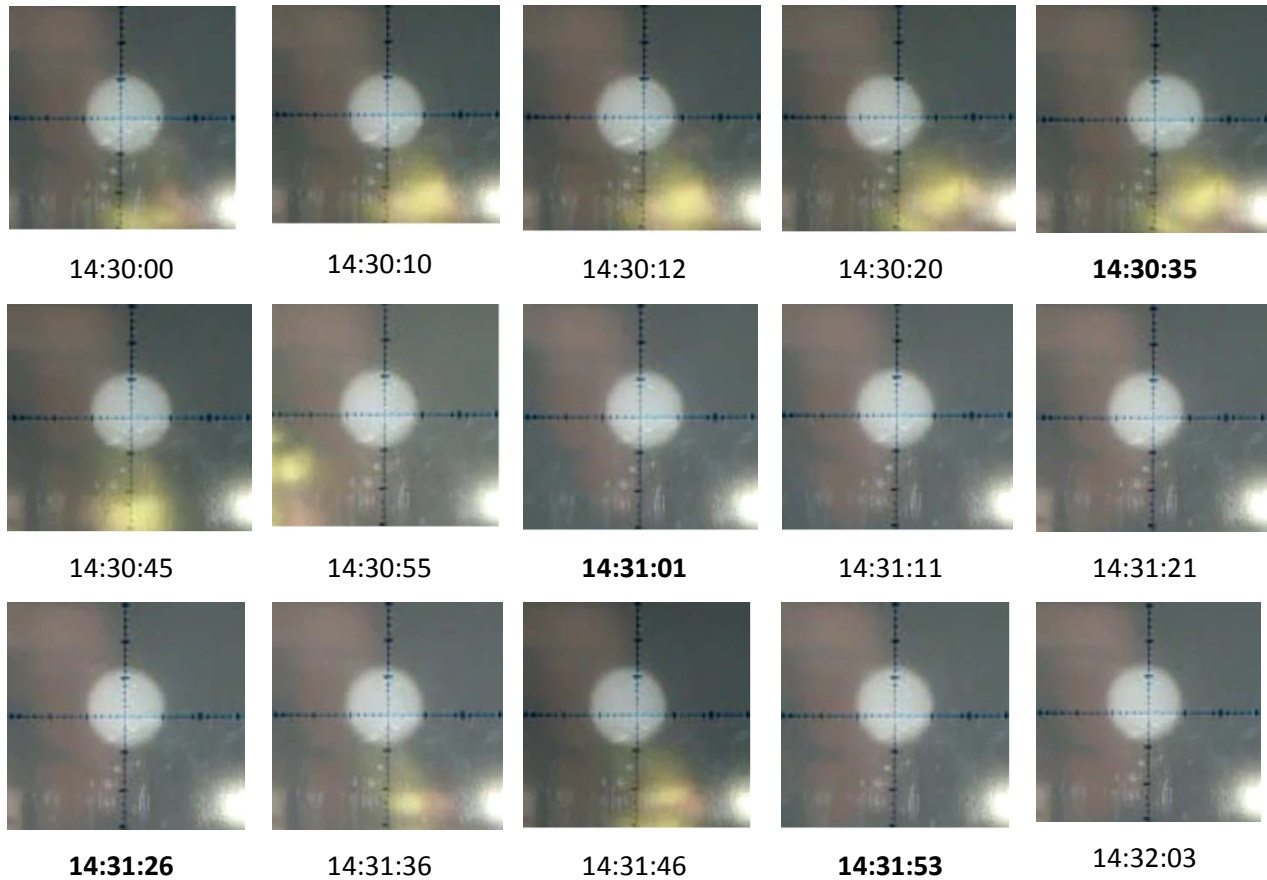


Table 5 - Heliostat in operation. Bold values indicate when a step was made. Only azimuth corrections can be seen here. Scale is in cm.

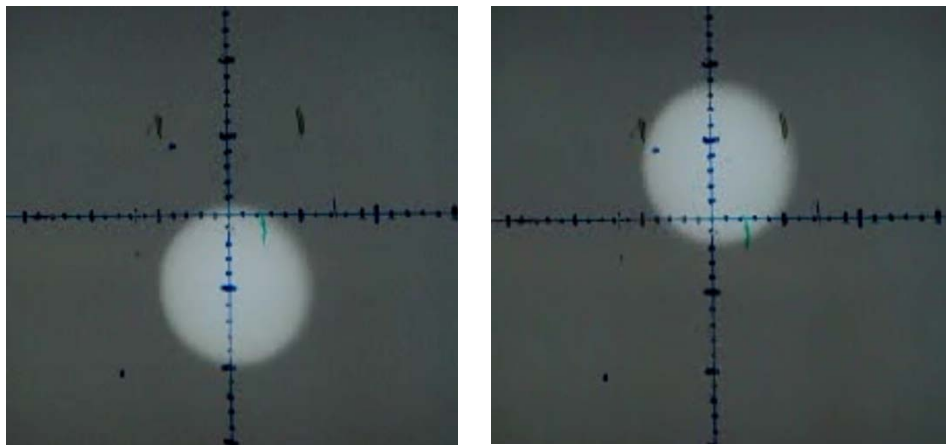


Table 6 – Heliostat Zenith angle correction



## 5 Discussion

The STS project was conducted to solve non-trivial problems in solar tracking. As can be seen from the work done, no specific tracking strategy was tested for feasibility, however the foundations were laid for experimental work to be began.

### 5.1 Algorithm Analysis

The algorithm analysis points out several interesting aspects of the algorithms tested. The purpose of this analysis was to approve the validity of the claims of the algorithm authors as well as to test the algorithms in a set of latitudes so the algorithm precision with latitude variation can be estimated.

The comparison of ENEA with SPA for the period of 2003-2023 deviates from the stated figures of the algorithm author, for the same temporal and spatial conditions. As can be seen in Figure 30, the maximum zenith deviation approaches 15 seconds of arc, whereas the results obtained by Grena (2007) show a max zenith angle deviation of ENEA with SPA of approximately 10 seconds of arc. Similar disagreements can be observed for azimuth and sun vector estimations. Table 4 summarizes the results.

The reason for these disagreements is potentially due to inaccurate coding done in the algorithm analysis.

Figure 33 depicts the mean deviation of the ENEA algorithm with the SPA algorithm for the period 2003-2023 for the range of latitudes between  $-65^\circ$  and  $65^\circ$  in steps of  $5^\circ$ . It can be seen, that around the equator, the algorithm produces its largest errors. This is in contradiction however to the expected results from sun vector calculation, in which one could assume that around the equator the sun elevation would be at its highest point on average, thus the sun vector error should be lowest, due to the cosine dependency in Equation 16.

Figure 34 shows the maximum sun vector deviation, which approximately follows the same bell shaped curve as the mean deviation. The standard deviation of ENEA with SPA can be seen in Figure 35, which shows, that around the tropics the standard deviation is largest.

Figure 36 points out the expected increase in the solar position estimation precision, as the elevation angle increases.

The ENEA algorithm was tested also in respect to the ephemeris data set and the resulting graphs, together with the results from the SPA vs. JPL estimation can be seen in Appendix C – Solar Position Deviations.

The SPA algorithm was tested against the JPL-ephemeris data set for the period 2010-2020 (Figure 62-67, Appendix C). The results of this test deviate by large from the statements of the authors of the algorithm, which are that the maximum error should not be larger than 1.008 arc seconds for the period between year -2000 to 6000. A very clear harmonic precision decrease can be observed after year 2011 to year 2020. However, for the year 2010-2011 the algorithm behaves as it is claimed.

The reason for the deviation might be inaccuracy in the ephemeris data set or a systematic error build up in the data handling algorithm.

## **5.2 SPTS System**

The general objectives for the SPTS system were achieved. Errors arose during system development, some of which were solved "on-the-way", whereas others still remain to be resolved.

### **5.2.1 Mechanical Design**

In the development stage of the SPTS system a large amount of choices regarding hardware, software and problem approach had to be made very carefully.

Mechanical system design and hardware chosen proved to be appropriate for the application.

Problems with the mechanical design of this prototype were:

1. Misalignment of zenith support structure with azimuth gearbox leading to a three-legged zenith axis support.

This problem was due to not-descriptive-enough drawings, which lead the technician machining the device to false conclusions. Precisely stated, the zenith axis support (Figure 20) consists of two rectangular plates and 8 pillars/columns and is located between the base-assembly and the zenith axis. The size of the plates was chosen in the drawings, so when the columns were mounted onto the base-assembly, they would not interfere with the azimuth gearbox. Detailed dimensions were not included in the drawings, which led to the three-legged design. The end product is however not influenced by this design error, since the zenith axis support was produced with very high rigidity.

Further development will require an azimuth optical encoder to be mounted onto the system. This encoder can be mounted onto the space left of the missing leg, hence the problem can be seen as a solution.

## 2. Large zenith-axis rotational resistance

Due to a slight misalignment of the zenith axis, the zenith gearbox and the rotational encoder, rotational resistance of the axis was observed. As a consequence of this resistance, the zenith motor was unable to drive the axis to a complete revolution.

The solution for this problem was found by tweaking the shaft connectors between gearbox, encoder and the axis.

## 3. System Leveling

The system had a dependency upon the geometry of the surface it is placed on. Solution was to mount three support-legs of adjustable height (bolts). This enables fast system calibration in the horizontal dimension.

## 4. Zenith Axis cabling

Due to the cabling of the zenith axis motor and rotary encoder, the degree of freedom for azimuth rotation is limited. A solution was found to mount a slip-ring assembly. Due to lack of time in combination with financial considerations, the slip-ring idea was dismissed and the decision was made to connect the zenith devices through cables of enough length, so as to enable a  $-180^{\circ}$  to  $180^{\circ}$  rotational range for the azimuth.

## 5. Motor calibration and optical alignment

Detection of axis movement with the naked eye was, if not impossible, very hard, thus motor calibration tests could not be performed. A solution was found to install a low power laser device on the zenith axis, so azimuth and zenith movement could be detected and measured onto a distant plane. The laser device was mounted so that it is adjustable in azimuth and zenith in its frame of reference. It was powered by the microcontroller.

### 5.2.2 Controller

The controller chosen for this system was the Rabbit® RCM5700W and its specifics can be seen in the datasheets attached to the project disk of this thesis (see Appendix A – Hardware). The controller was chosen because of its capability to communicate with a server connected to the same network. In this way the controller could be programmed with general hardware interface codes, whereas the server was aimed to be the sun-algorithm computing machine.

The aimed controller-server interaction was achieved successfully. The server was programmed to respond to a specific request, containing position and time data, with the ENEA algorithm results. The controller was programmed to prepare the request, send it in specific time intervals and work with the data received. The interaction rate was set at 10Hz and the system seemed to be operating at it at most times.

Problems arose when the controller was programmed to interact with the azimuth motor in half step mode and the server communication was disrupted. The reason for the disruption was found to be, that because specific bits controlling the motor also were the gateway for the server communication. The problem was not realized in the initial stages of project development, since only the Full-Step cycle was adopted then, and the Full-Step cycle fires each bit individually, whereas the half-step cycle is working in a parallel mode, thus disrupting the default functionality of the port. A partial solution was found to leave the azimuth motor working in full step mode, whereas the zenith was controlled in half step.

A problem with the rotary encoder of the system was encountered and it was not used in the final experimental work. The reason for the problem is again inaccurate management and programming of the controllers input/output ports.

### 5.3 Suggestions for Future Work

The steps of hardware and software improvements that can be suggested as of time of writing are:

1. Slip Rings – Mounting the slip rings will enable the zenith axis to have a full rotational degree of freedom and will increase system lifetime.
2. Create PCB for the system and install into the base assembly
3. Rearrange the rabbit ports so that interrupts, motor control and server interactions do not interfere – The first step that should be done is to rearrange the ports so, that to control both motors through the same port. The interrupts and the server interaction need to be synchronized, since both work through the same port on the controller.
4. Mount Solar cell device onto zenith axis
5. Create an array of light sensors for active tracking and write the tracking logic for the system
6. Check algorithm analysis toolbox for errors and repeat the algorithm analysis toolbox
7. Analyze the rest of the algorithms written
8. Increase the time period of analysis
9. Add algorithms to the server
10. Create a Web User Interface

### 5.4 Suggestions for Experiments

The suggested experimental work consist of:

1. Device Calibration:
  - a. Conduct an experiment with the device throughout a defined time period with a precise algorithm.
  - b. Create a virtual model and simulate under the same conditions by comparing the solar cell output with an estimated output based on spectral properties of the cell and a clear sky analysis.
  - c. Conduct an experiment under same conditions with a random error of certain mean and standard deviation
  - d. Compare the (3) with (1) and (2).
2. Solar Cell Experiments
  - a. Install different solar cells and compare output with models and reference solar cell
  - b. Establish spectral properties of solar cells

- c. Establish temperature dependencies
  - d. Establish tracking precision requirements – influence of incidence angle upon output
- 3. Heliostat Experiments
  - a. Test different heliostat tracking algorithms
- 4. CPV experiments

By going through the steps described in (1) – Device Calibration, the system and model can be calibrated. Having a precise model that agrees with system output at any time, one can estimate cell behavior, and specifically the impact of tracking precision onto output, if the cell's spectral response is known. Otherwise, the cells spectral response can be established by conducting steps one through four and comparing with the reference model.

In this way, a real-time solar cell experimental apparatus can be developed. The computational intensity of such a system will not be a source of problem, since the server can perform the real-time radiation and spectral distribution estimations, and compare them with system output, knowing the exact orientation of the cell.

In a heliostat setup, the system could be used to test the validity of different heliostat tracking techniques. However, since the beam falling onto the target comes theoretically always from the same direction, the beam could be focused and CPV cells could be tested.

Having a precise positioning device working in combination with a calibrated solar cell and a good agreement with a model, one could perform radiation estimations.

## 6 Conclusions

The system build for Solar Tracking Strategies analysis consists of an experimental apparatus and an analytical analysis toolbox. A unique server-microcontroller configuration was chosen for system control. This configuration proved to be highly adaptable, maintainable and has the potential to increase system flexibility to very high levels.

The algorithm analysis conducted is to a certain degree inconclusive, since errors obtained deviate from the stated errors of the authors of the algorithms. However, errors produced by the algorithms written in this project are not sufficient to influence the total system positioning precision to a large degree. Further work will include analysis of simplest equation of time and declination angle based algorithms to the most computationally intensive ones. Several characteristics of each algorithm can be derived, such as precision variation with time and latitude, and computational cost. The results of this analysis can point towards specific algorithms when decisions upon tracking applications are being made.

The local frames of reference were found for the experimental setup using the Google Earth® software package. Their level of precision was computed to be sufficient and to influence the final system precision to a minor extent.

The system positioning tests conducted and in specific the heliostat experiments prove the applicability of the hardware, software and the methodology adopted. However, it was operating in a very controlled environment and still a large number of improvements need to be made in software and hardware.

Final system solar positioning precision was determined to be  $0.2398^\circ$ . Heliostat tests showed a system precision of  $0.1719^\circ$ .

## Works Cited

- [1] HORIZONS, Jet Propulsion Laboratory, Solar System Dynamics. [Online]. <http://ssd.jpl.nasa.gov/horizons.cgi>
- [2] Ibrahim Reda, Afshin Andreas. (2008, Jan.) National Renewable Energy Laboratory. [Online]. <http://rredc.nrel.gov/solar/codesandalgorithms/spa/>
- [3] R. Grena, "An algorithm for the computation of the solar position," *Solar Energy*, vol. 82, pp. 462-470, 2008.
- [4] Abengoa Solar. [Online]. [http://www.abengoasolar.com/corp/web/en/technologies/concentrated\\_solar\\_power/parabolic\\_trough/index.html](http://www.abengoasolar.com/corp/web/en/technologies/concentrated_solar_power/parabolic_trough/index.html)
- [5] SolarPACES. Solar Parabolic Trough. [Online]. [http://www.solarpaces.org/CSP\\_Technology/docs/solar\\_trough.pdf](http://www.solarpaces.org/CSP_Technology/docs/solar_trough.pdf)
- [6] K.K. Chong, C.W. Wong, "General formula for on-axis sun-tracking system and its application in improving tracking accuracy of a solar collector," *Solar Energy*, pp. 298-305, 2009.
- [7] William B. Stine, Michael Geyer. (2001) Power From the Sun. [Online]. <http://www.powerfromthesun.net/book.htm>
- [8] Marcelino Sánchez, Manuel Romero, "Methodology for generation of heliostat field layout in central receiver systems based on yearly normalized energy surfaces," *Solar Energy*, vol. 80, no. 7, pp. 861-874, 2006.
- [9] Y. T. Chen, A. Kribus, B. H. Lim, C. S. Lim, K. K. Chong, J. Karni, R. Buck, A. Pfahl, T. P. Bligh, "Comparison of Two Sun Tracking Methods in the Application of a Heliostat Field," *ASME JOURNAL OF SOLAR ENERGY ENGINEERING*, vol. 126, Feb. 2004.
- [10] MANUEL BLANCO-MURIEL, DIEGO C. ALARCO´N-PADILLA, TEODORO LO´PEZ MORATALLA, MART´IN LARA-COIRA, "COMPUTING THE SOLAR VECTOR," *Solar Energy*, vol. 70, no. 5, pp. 431-441, 2001.
- [11] T. P. Chang, "The Sun's apparent position and the optimal tilt angle of a solar collector in the northern hemisphere," *Solar Energy*, no. 83, pp. 1274-1284, 2009.
- [12] Marion Schroedter-Homscheidt, Jethro Betcke, Detlev Heinemann, Susanne Heinicke, Elke Lorenz, Sibylle Petrak, Thomas Holzer-Popp, Lucien Wald, "ENERGY-SPECIFIC SOLAR RADIATION DATA FROM MSG: THE HELIOSAT-3 PROJECT," Deutsches Zentrum für Luft- und Raumfahrt e.V. (DLR), Deutsches Fernerkundungsdatenzentrum (DFD), Universität Oldenburg, Abteilung Energie- und Halbleiterforschung, 2006.
- [13] Jun Qin a,†, Zhuoqi Chen b, Kun Yang a, Shunlin Liang c, Wenjun Tang a, "Estimation of monthly-mean daily global solar radiation based on MODIS and TRMM products," *Applied Energy*.
- [14] European Solar Radiation Atlas. [Online]. <http://www.helioclim.org/esra/>
- [15] Jong-Min Yeom a,1, Kyung-Soo Han b,n, "Improved estimation of surface solar insolation using a neural network and MTSAT-1R data," *Computers & Geosciences*.
- [16] A. Goetzberger, V.U. Hoffmann, *Photovoltaic Solar Energy Generation*. Springer.



- [17 Klaus Wyser\*, William O'Hirok, Catherine Gautier, Charles Jones, "Remote sensing of surface solar irradiance with corrections for 3-D cloud effects," *Remote Sensing of Environment*.
- [18 Annette Hammera, Detlev Heinemann, Carsten Hoyera,\*, Rolf Kuhlemann, Elke Lorenza, Richard Müller, Hans Georg Beyer, "Solar energy assessment using remote sensing technologies," *Remote Sensing of Environment*, vol. 423-432, 2003.
- [19 John A. Duffie, William A. Beckman, *Solar Engineering of Thermal Processes*, Third Edition ed. USA: WILEY, 2006.
- [20 Rigollier C., Lefèvre M., Wald L.\*, "The Method HELIOSAT-2 for deriving shortwave solar radiation from satellite images," *Solar Energy*, vol. 77, pp. 159-169, 2004.
- [21 R. R. D. Center. (2000, Feb.) NREL, SOLPOS. [Online]. <http://redc.nrel.gov/solar/codesandalgorithms/solpos/>
- [22 Editorial, "Reporting solar cell efficiencies in Solar Energy Materials," *Solar Energy Materials & Solar Cells* 92, pp. 371-373, 2008.
- [23 L. Petrov. (2009, Sep.) Solar Tracking Strategies. [Online]. [www.sts.ustrem.org/pages](http://www.sts.ustrem.org/pages)
- [24 SolFocus CPV cells. [Online]. <http://www.solfocus.com/en/technology/>

## 7 Appendix A - Hardware

### 7.1 Controller

For this project, the Rabbit RCM5700W was recognized as a viable microcontroller to be used.



**Figure 37 – RCM5700W Rabbit with the Rabbit 5000 Core**

This controller has the following general features:

1. Compact module in Mini PCI Express format – The format enables ease of integration into developed boards through a 52-pin mini PCI Express socket.
  - a. Size – (30mm x 51mm x 3mm)
  - b. Up to 35 general purpose input-output lines each with up to four configurable alternate functions
  - c. 3.3V supply – compatible to standard USB
  - d. Six CMOS-compatible serial ports
2. Rabbit 5000® CPU

- a. Operating Speed – Up to 50.0MHz
  - b. Two clocks – main oscillator and RTC
- 3. 10/100Base-T Ethernet enabled
  - a. PHY interface, enabling automatic detection of cross-over or regular straight-through cable is used
- 4. 128kB on-chip SRAM and 1MB of flash memory

The module was chosen instead of the wireless enabled RCM5600W module, due to faster developing speeds it can provide. Compilation of the libraries for the wireless enabled module does take up to a minute and in the code development phase, compilation of code is being conducted several tens of times during a day. This alone adds up to a large amount of time saved, by choosing the Ethernet enabled module instead of the wireless module. Another positive aspect of the RCM5700W module was that connectivity problems with the wireless networks around Dundee University Campus were circumvented.

The datasheet for the model can be found on the ***Project Disc*** provided as part of this work, under ***Home->Datasheets->Rabbit RCM5700W Product Manual.***

## 7.2 Display

The display used was the NewHeaven NHD-0420DZ-FL-YBW-3V3 with the built-in SPLC780D-01 display controller. The display is a 4 line, 20 character alphanumeric display and serves the manual user interface functionalities. The display has a power consumption of approximately 200mA with the backlight on, at 3.3V. Details regarding the display and its controller can be found on the ***Project Disc*** at ***Home->Datasheets->Display*** and ***Home->Datasheets->SPLC780D Display Controller.***

## 7.3 Motors & Gearboxes

The motors chosen for this project were the RS332947 7.5° unipolar stepper motors. The motors have the following general specifications:

- 1. Power Consumption    2W;
- 2. Max. Pull-In rate       350 steps/s;
- 3. Temperature Range    -20° - 70°;
- 4. Step Angle               7.5°;
- 5. Step Angle Tolerance    $\pm 0.6667^\circ$ ;

The motors proved to be very reliable during the testing and experimental stage of the project. They have been operated by use of a pair of ULN2003 Darlington Transistor Arrays and a 240/12V 500mA AC/DC transformer. The motors were operated without the use of drivers. Throughout testing periods of letting the motors run at high speed or stay still with max detent torque, the temperature of the housing of the motors did not reach very high levels ( $>50^{\circ}$ ), as touching the motors with bare hands indicated. For detailed motor information, the supplied Motor&Gearbox datasheet can be seen from the **Project Disk** at **Home->Datasheets->Stepper Motor and Gearbox Datasheet** and the datasheet for the Darlington Array ULN2003 is at **Home->Datasheets->ULN 2003 Darlington Transistor Array**.

## 7.4 PHP Server

Two PHP servers were used for the project. The first server was a web-connected server and served as the actual application demonstration server, whereas the second server was installed on the machine that was used for the development of the entire project, including all the different programming environments for microcontroller and web programming. Having the server as a localhost, enables faster project development, since any modification made onto the PHP®, XML®, HTML®, JAVASCRIPT® or Dynamic C® code was immediately active, without having to update the web server.

The PHP localhost was installed on a Windows 7® PC. Further development on a different machine will be possible if an equivalent of the Internet Information Services 7® (IIS7) localhost capabilities is installed with a PHP extension.

The procedures for installing the PHP server on the Windows 7® platform are the following:

1. Install the IIS7 from the official web-site – 180 day trial available. (<http://www.iis.net/>)
2. Install the PHP extension for IIS7 and follow the instructions (<http://php.iis.net/>)
3. Install the PHP Manager extension for IIS7 and follow instructions (<http://phpmanager.codeplex.com/>)

To proceed developing the project, the contents of the **Project Disk** need to be copied into the *wwwroot* directory of the IIS7 program. Please see **Project Disk-> readme.txt** for further information.

## 8 Appendix B - Software

In order to keep this thesis in reasonable physical dimensions, this appendix points towards the links at the STS web-Page, where the Algorithms used can be downloaded, and gives the essential information needed while reading the thesis.

### 8.1 MATLAB

The MATLAB® environment was employed for the computational analysis of the AAs. The choice for this environment was made due to its many beneficial characteristics, such as:

1. **Very High Level Environment allowing Object Oriented Programming approaches** - Due to the repeatability of many internal AA functions, the OOP techniques used shortened the workload and strengthened the organization of the analysis. The high level MATLAB language allowed for fast code implementation using dry mathematical information from different authors.
2. **Graphical User Interface** – Being able to graphically illustrate the results of a computation was a major benefit for using MATLAB. The GUI build for use of MATLAB enables user interaction with the variables of a computation in a fast and intuitive manner.
3. **Support** – The MATWORKS support forum was useful for the development process of the algorithms, partly with suggestions to solve problems, but also with written .m code supplied at no charge (SPA.m developed by Vincent Roy).

#### 8.1.1 Solar Position Algorithm Analysis Toolbox (SPAAT)

SPAAT was begun with the aim of a complete solar engineering analysis toolbox to analyze solar position and radiation algorithms. However, due to the large amount of work involved, the toolbox was developed to perform only solar position algorithm analysis so far. The complete toolbox is available zipped at the **Project Disk** at **Home->Source Code->SAT toolbox**. It can be immediately implemented with the only requirement of MATLAB 7 or newer. Please bear in mind that all code within this toolbox is in development stage and is therefore not bug free!

#### 8.1.2 SPA

The Solar Position Algorithm developed by Ibrahim Reda and Afshin Andreas on behalf of the National Renewable Energy Laboratory (NREL) is as of knowledge of the author of this work at the time of writing, the most precise solar position algorithm with a precision of  $\pm 0.0003^\circ$ . The range of validity for the algorithm is from year -2000 to 6000.

The .m code for SPA can be found on the **Project Disc** at **Home->Source Code->SPA.m**.

### 8.1.3 ENEA

This algorithm was developed by Roberto Grena at Italian National agency for new technologies, Energy and sustainable economic development – ENEA. The claimed precision [3] is  $0.0027^\circ$  and the decrease in amount of computations performed is of the order of three magnitudes, in comparison to SPA [3]. The algorithm is however valid only for the time range between year 2003 and 2023.

The .m code for ENEA can be found on the ***Project Disc*** at ***Home->Source Code->ENEA.m***.

### 8.1.4 JPL

This code was developed to interpolate between the reference ephemeris data [1] and to generate error matrices of the algorithms tested. For the actual positioning tests conducted in this work, no interpolation was performed.

The .m code for JPL can be found on the ***Project Disc*** at ***Home->Source Code->JPL.m***.

## 8.2 Dynamic C

The code developed in this environment was written with the idea of creating robust flexible functions for general use with every component the code was written for. Detailed descriptions were attempted at all libraries and functions within the code, so as to enable future work on the SPTS system without many complications.

When in the Dynamic C environment, if any function seems unclear, holding the control button (*ctrl*) and pressing H button, will deliver an explanation of the function, if such is existing.

### 8.2.1 Libraries

#### 8.2.1.1 SPC780D – Display Library

This library was created for use with the SPLC780D microcontroller and the NewHeaven Display NHD 0420DZ FL YBW 3V3. The library is optimized and did undergo a series of upgrades in order to become functional and bug-free.

The .lib code for the library can be found on the ***Project Disc*** at ***Home->Source Code->Display Library***

#### 8.2.1.2 SM332947 – Stepper Motor Library

This library was developed for use with the unipolar stepper motors RS332947. The functions within the library account for backlashes of the gearboxes the motors are connected to, and do to a large extend substitute any ready build driver for these stepper motors motion control. For further information see

***Project Disc*** at ***Home->Source Code->Stepper Motor Library***.

### **8.2.1.3 SPTS – SPTS system library**

This library contains functions to work with the rabbit RTC, Interrupts and server interactions. For detailed description, see the source file at ***Project Disc at Home->Source Code->SPTS Library.***

## **8.2.2 Source Code**

### **8.2.2.1 Main File**

This is the file that combines the libraries and functionalities used for experimentation. This file is very high level and it should be relatively simple for future students to create equivalent source files to this one, so as to control the SPTS system. See ***Project Disc at Home->Source Code->SPTS Main File.***

## **8.3 HTML and JavaScript**

These source codes can be seen from any browser that is used for the project.

### **8.3.1 JavaScript**

### **8.3.2 PhP**

The PHP file used for the solar position computation can be seen at ***Project Disc at Home->Source Code->Solar Position Calculator in PHP.*** This source file contains the necessary logic to be able to respond to the rabbit requests and computes the solar position only through the ENEA algorithm. For further work, other algorithms can be implemented.

## 9 Appendix C - Solar Position Deviations

### 9.1 Variation of Solar Azimuth and Elevation with deviations in declination, hour angle and latitude

#### 9.1.1 Latitude ( $\varphi$ )

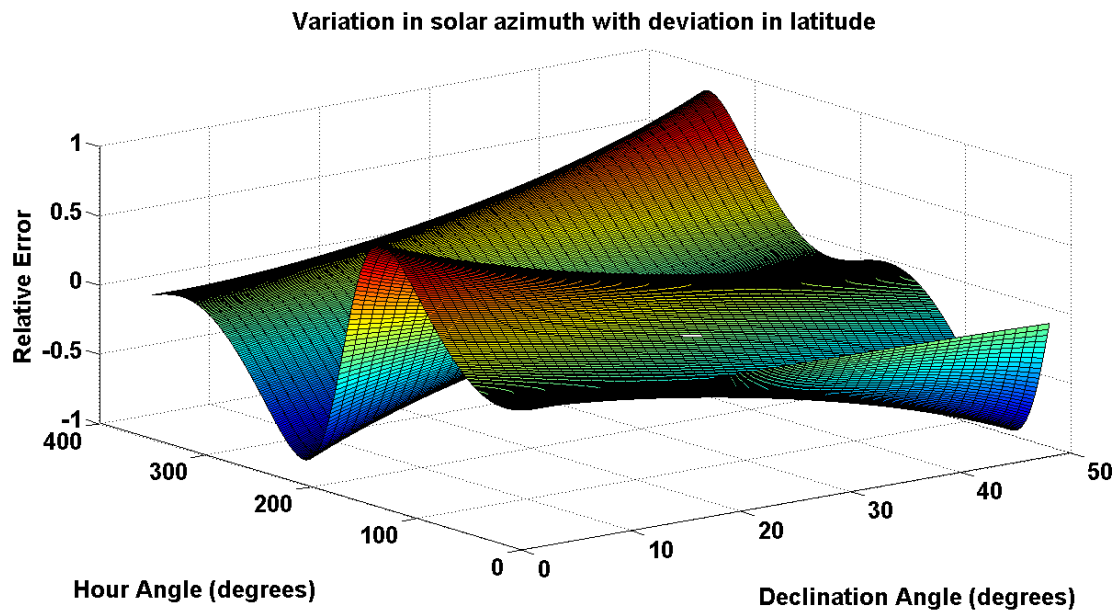


Figure 38 – Variation (relative) in solar elevation angle with deviation in Latitude. The x axis being the hour angle variation throughout a day ( $0^\circ$  to  $360^\circ$ ), the y-axis the declination angle variation ( $-24^\circ$  to  $24^\circ$  - denoted from 0 to 48 on the graph).



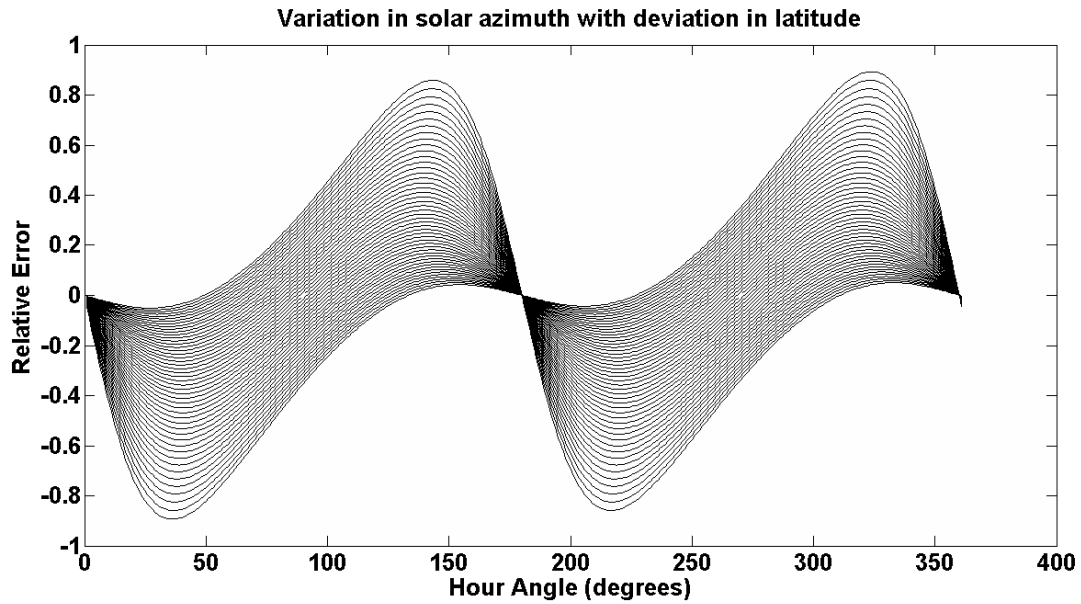


Figure 39 - Variation (relative) in solar azimuth angle with deviation in latitude angle. The x-axis shows the hour angle variation throughout a day ( $0^{\circ}$  to  $360^{\circ}$ ). The declination angle variation ( $-24^{\circ}$  to  $24^{\circ}$ ) can be seen as the superimposed lines.

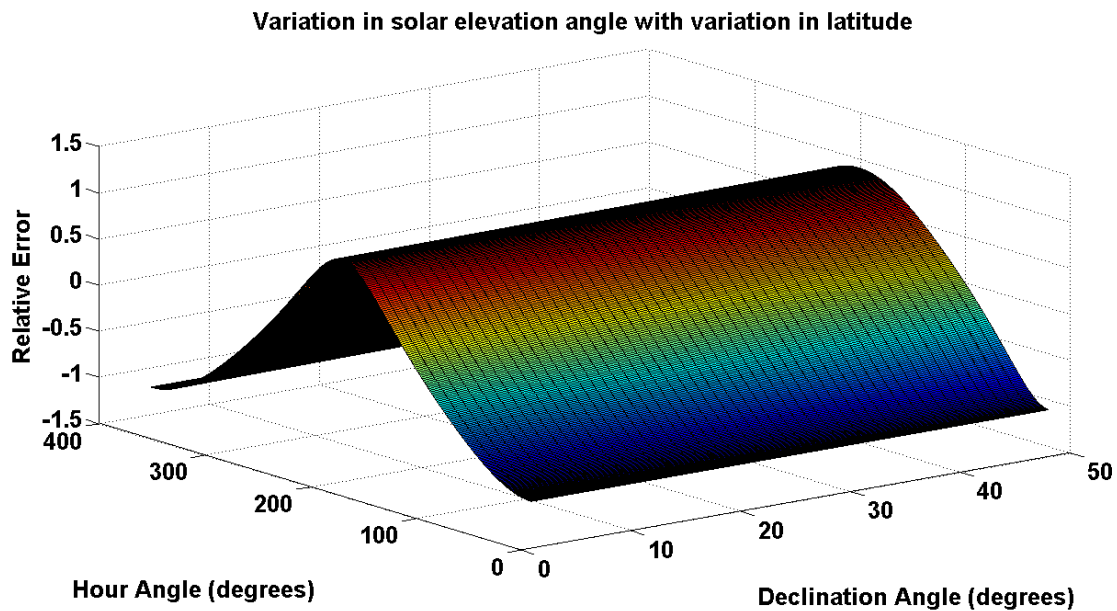
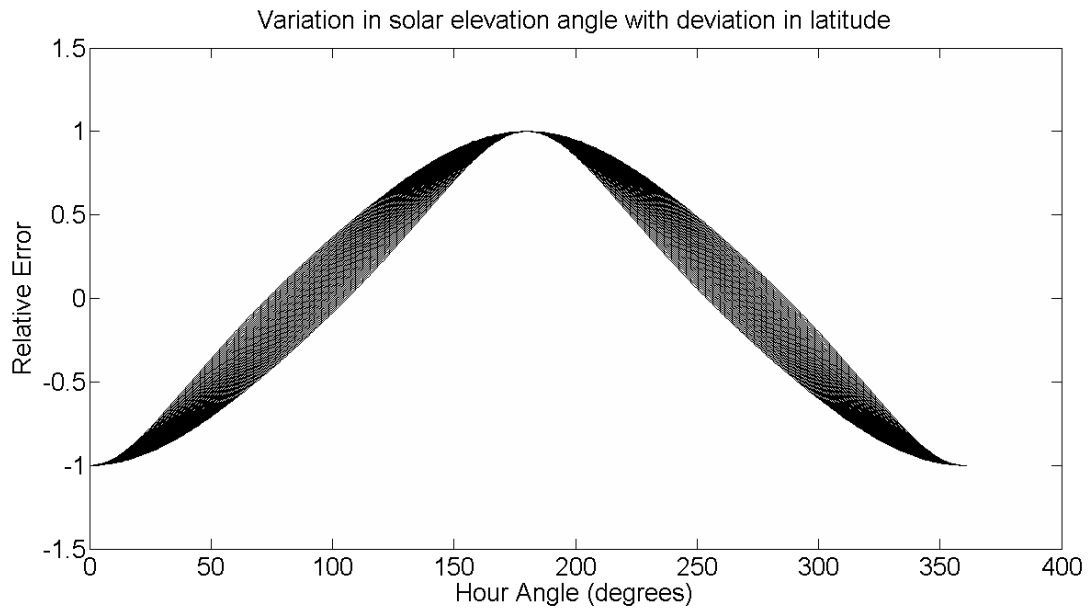


Figure 40 - Variation in solar azimuth angle with deviation in latitude. The x axis being the hour angle variation throughout a day ( $0^{\circ}$  to  $360^{\circ}$ ), the y-axis the declination angle variation ( $-24^{\circ}$  to  $24^{\circ}$  - denoted from 0 to 48 on the graph).



**Figure 41 - Variation (relative) in solar elevation angle with deviation in latitude angle. The x-axis shows the hour angle variation throughout a day (0° to 360°). The declination angle variation (-24° to 24°) can be seen as the superimposed lines.**

### 9.1.2 Declination

Variation in solar elevation angle with deviation in declination angle

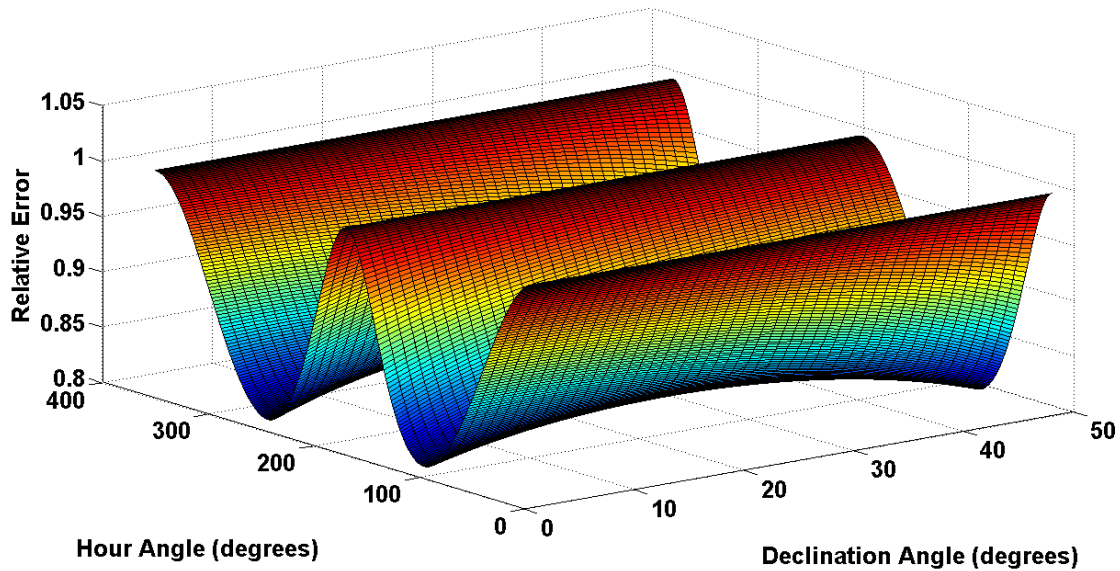


Figure 42 - Variation (relative) in solar elevation angle with deviation in declination angle. The x axis being the hour angle variation throughout a day ( $0^\circ$  to  $360^\circ$ ), the y-axis the declination angle variation ( $-24^\circ$  to  $24^\circ$  - denoted from 0 to 48 on the graph).

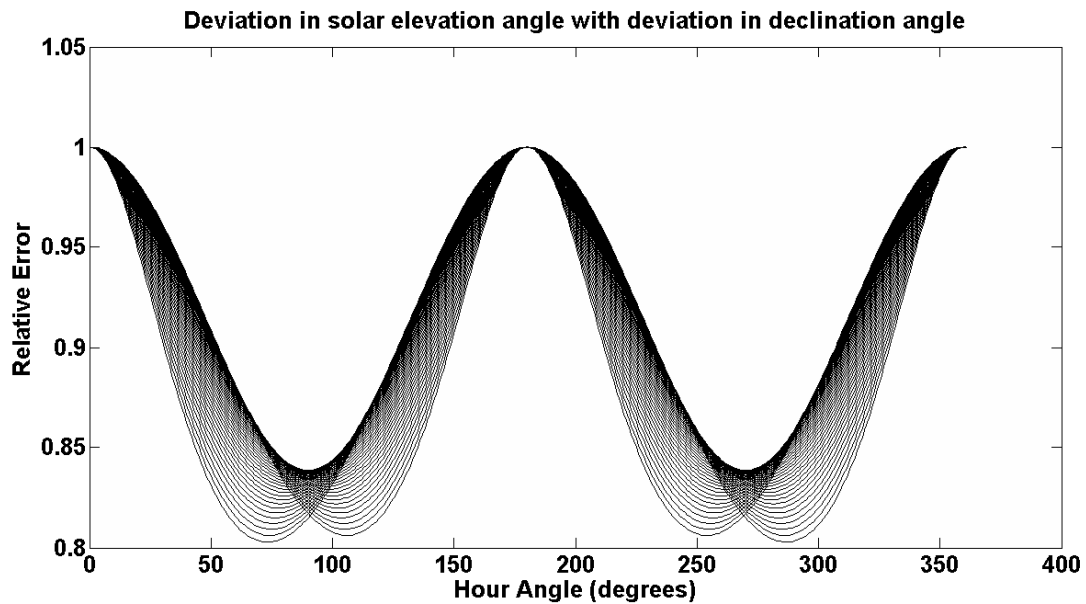


Figure 43 - Variation (relative) in solar elevation angle with deviation in declination angle. The x-axis shows the hour angle variation throughout a day ( $0^\circ$  to  $360^\circ$ ). The declination angle variation ( $-24^\circ$  to  $24^\circ$ ) can be seen as the superimposed lines.

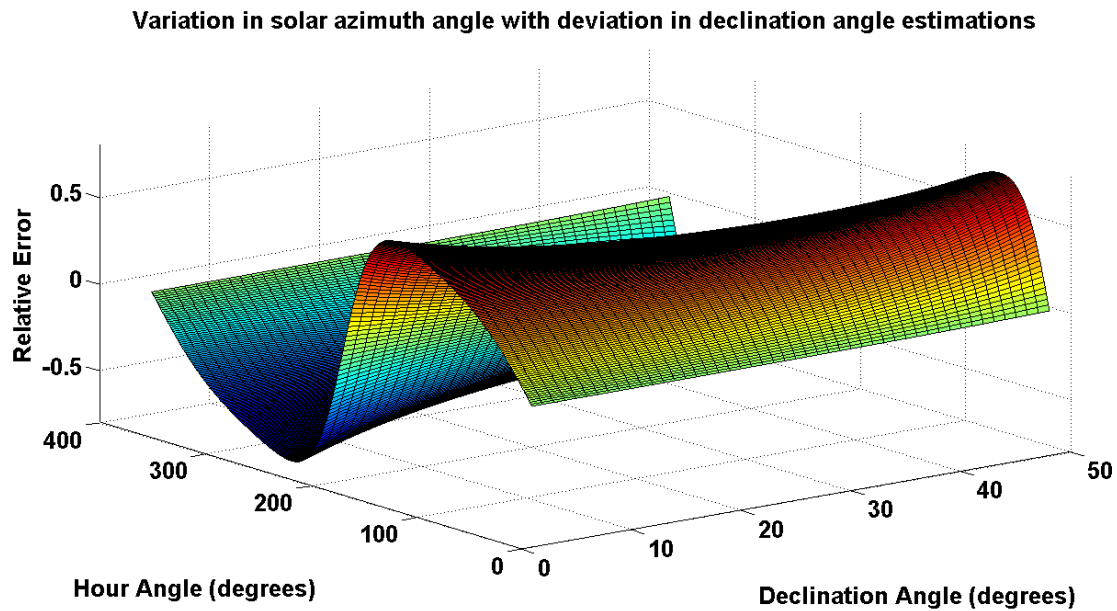


Figure 44 - Variation (relative) in solar azimuth angle with deviation in declination angle. The x axis being the hour angle variation throughout a day ( $0^{\circ}$  to  $360^{\circ}$ ), the y-axis the declination angle variation ( $-24^{\circ}$  to  $24^{\circ}$  - denoted from 0 to 48 on the graph).

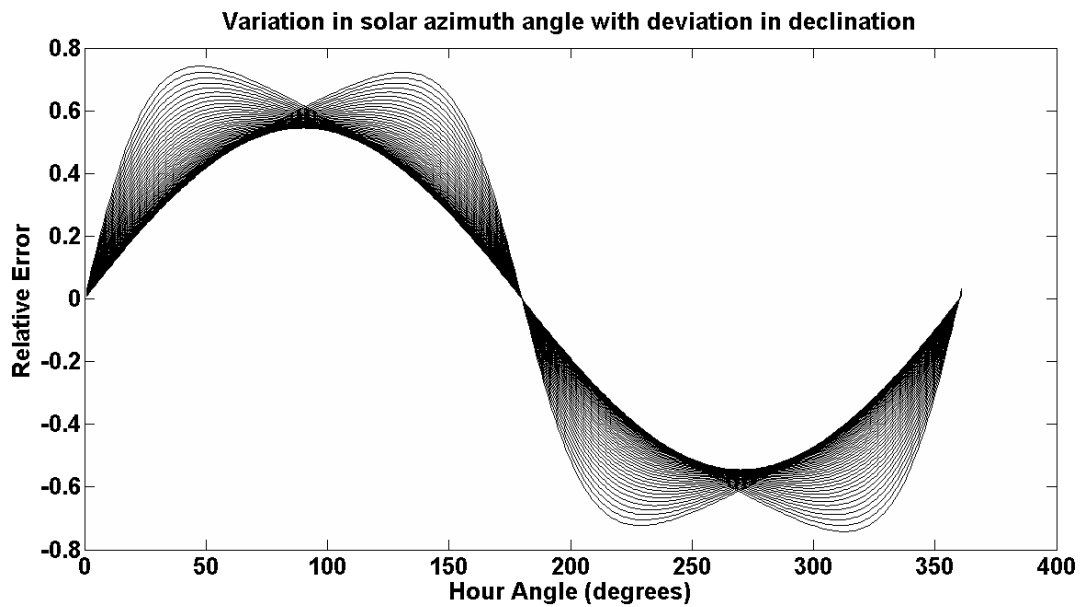


Figure 45- Variation (relative) in solar azimuth angle with deviation in declination angle. The x-axis shows the hour angle variation throughout a day ( $0^{\circ}$  to  $360^{\circ}$ ). The declination angle variation ( $-24^{\circ}$  to  $24^{\circ}$ ) can be seen as the superimposed lines.

### 9.1.3 Hour Angle

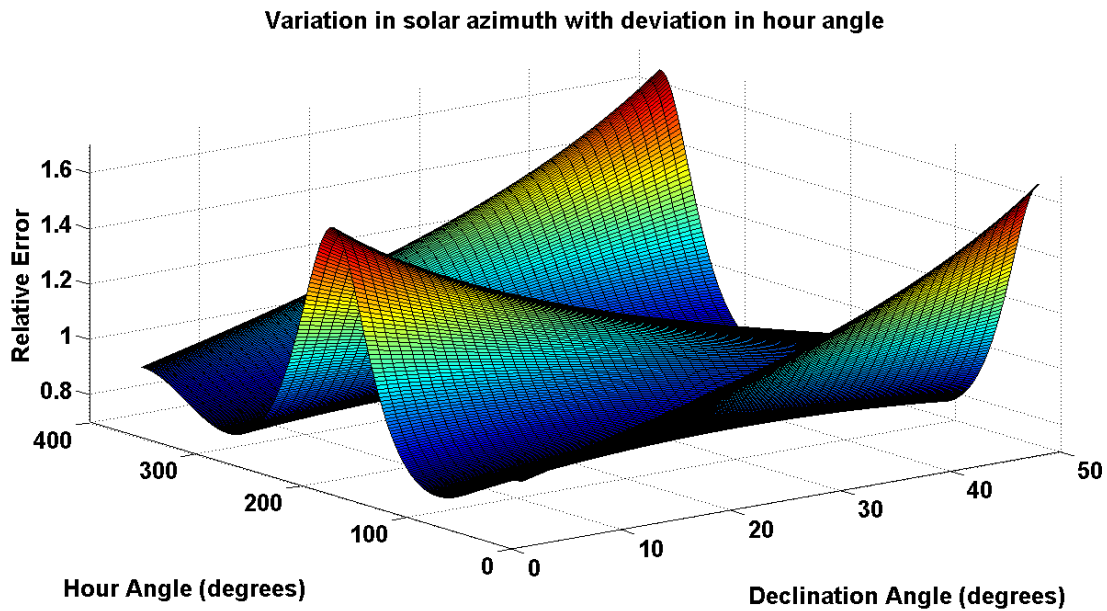


Figure 46 - Variation (relative) in solar azimuth angle with deviation in hour-angle. The x axis being the hour angle variation throughout a day ( $0^{\circ}$  to  $360^{\circ}$ ), the y-axis the declination angle variation ( $-24^{\circ}$  to  $24^{\circ}$  - denoted from 0 to 48 on the graph).

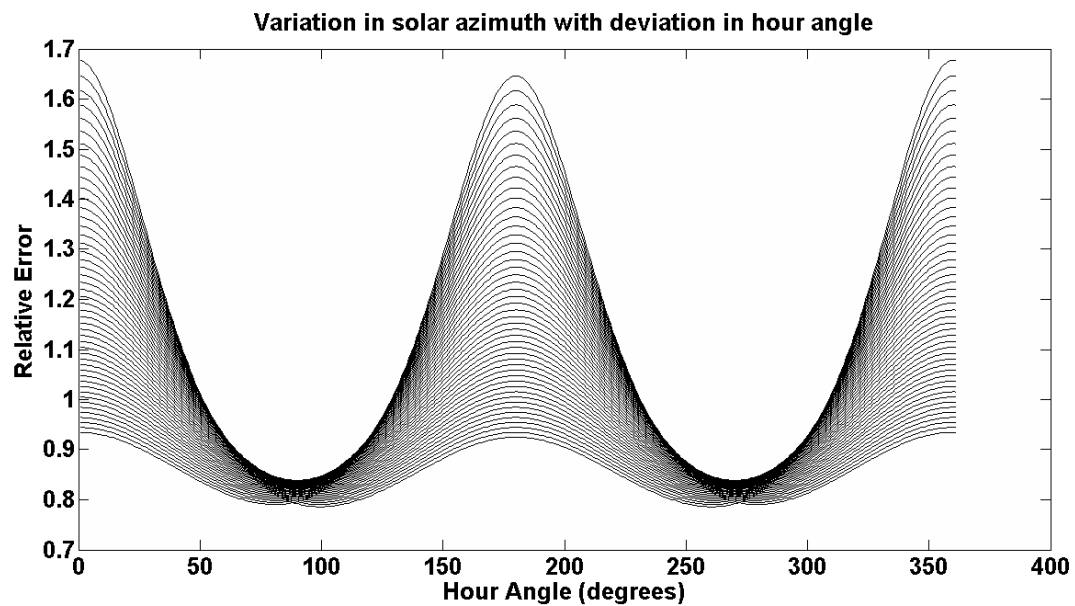


Figure 47 - Variation (relative) in solar azimuth angle with deviation in hour-angle. The x-axis shows the hour angle variation throughout a day ( $0^{\circ}$  to  $360^{\circ}$ ). The declination angle variation ( $-24^{\circ}$  to  $24^{\circ}$ ) can be seen as the superimposed lines.

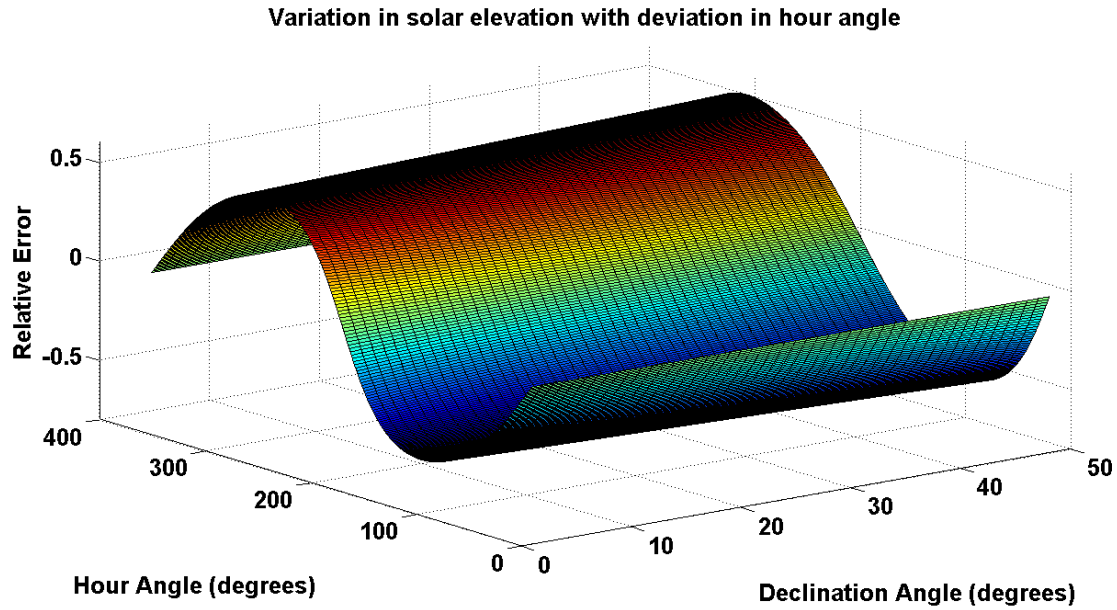


Figure 48 - Variation (relative) in solar elevation angle with deviation in hour-angle. The x axis being the hour angle variation throughout a day ( $0^{\circ}$  to  $360^{\circ}$ ), the y-axis the declination angle variation ( $-24^{\circ}$  to  $24^{\circ}$  - denoted from 0 to 48 on the graph).

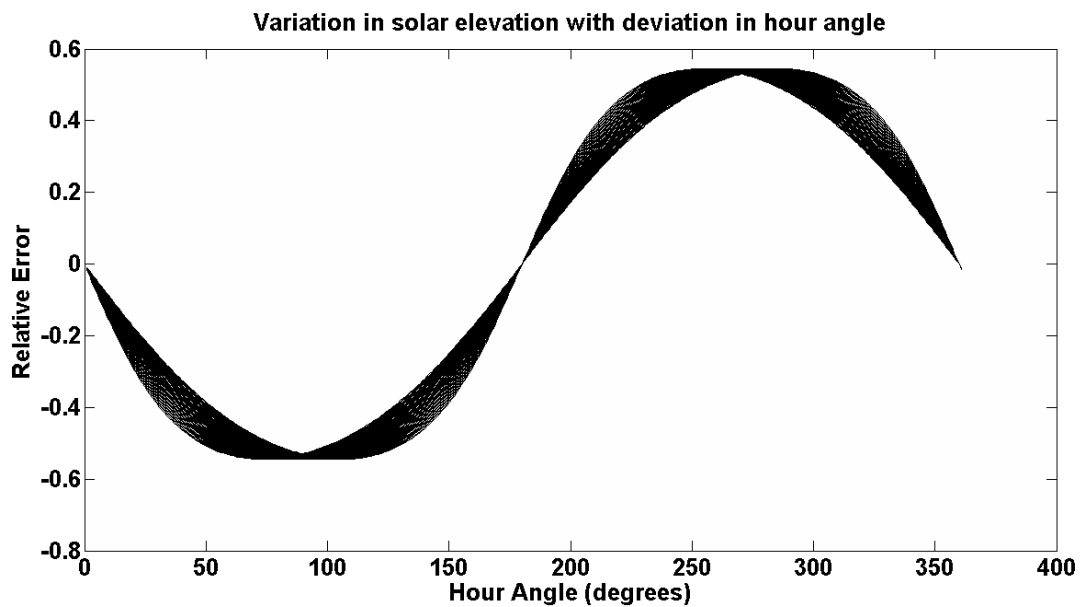


Figure 49 - Variation (relative) in solar elevation angle with deviation in hour-angle. The x-axis shows the hour angle variation throughout a day ( $0^{\circ}$  to  $360^{\circ}$ ). The declination angle variation ( $-24^{\circ}$  to  $24^{\circ}$ ) can be seen as the superimposed lines.

## 9.2 Variations in Heliostat positioning estimations due to deviations in Sun Position

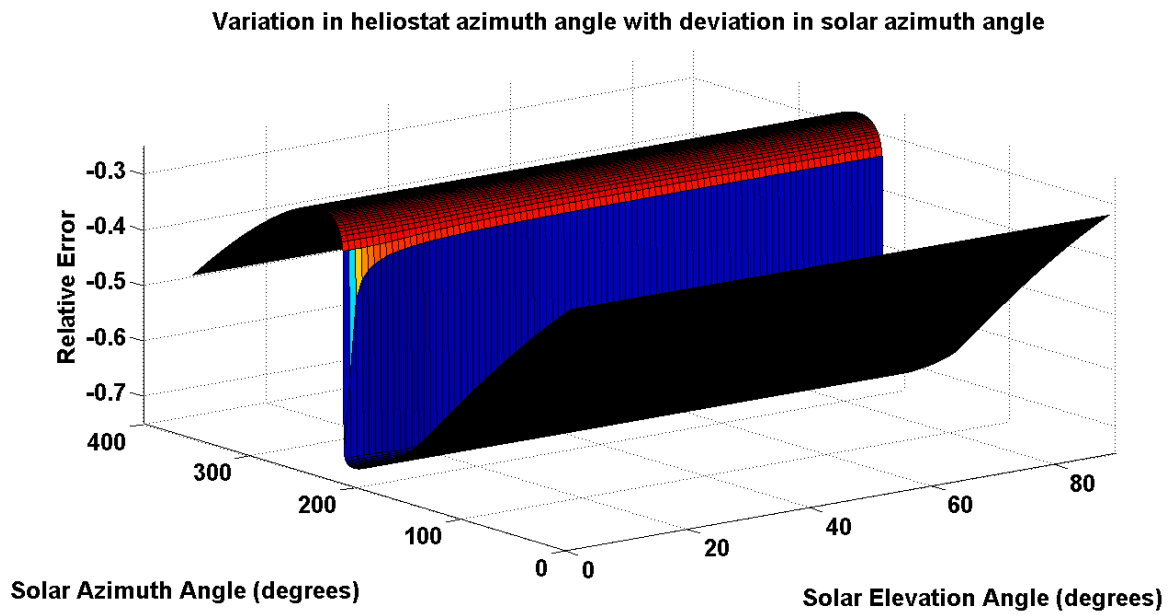


Figure 50 – Variation in heliostat azimuth positioning precision with deviation in solar azimuth angle ( $\Phi = 143.2, \lambda = 1.64$ )

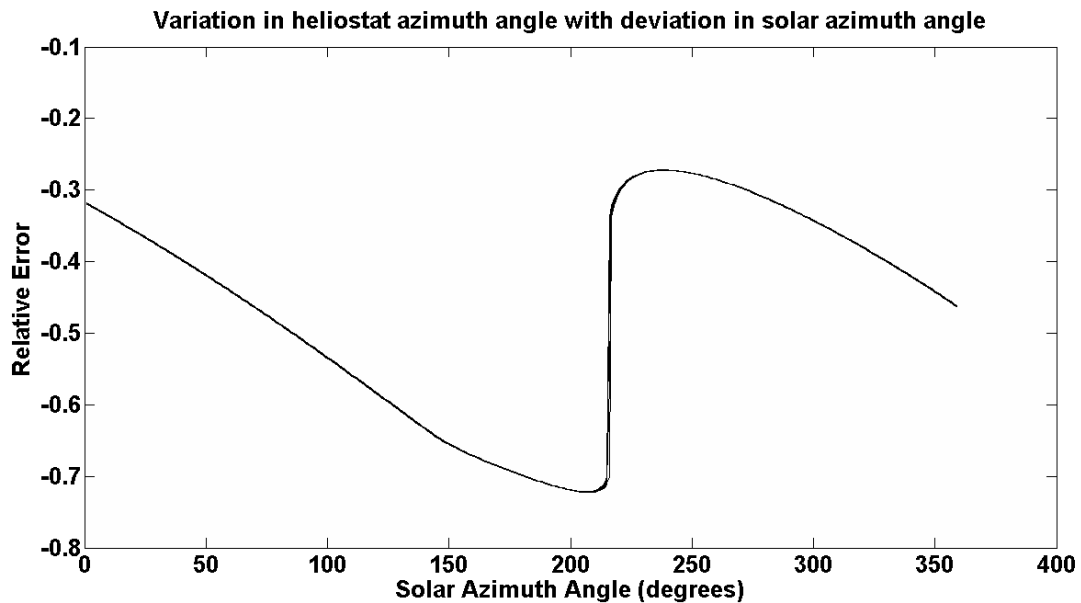


Figure 51 - Variation in heliostat azimuth positioning precision with deviation in solar azimuth angle (2D- sun elevation influence is negligible). ( $\Phi = 143.2, \lambda = 1.64$ )

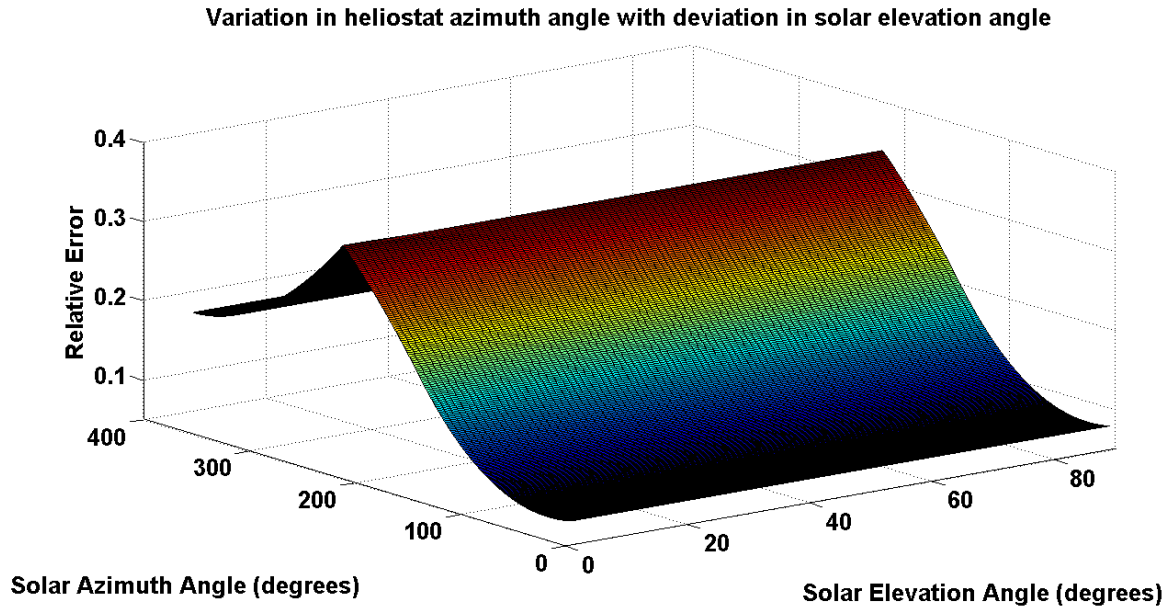


Figure 52 - Variation in heliostat azimuth positioning precision with deviation in solar elevation angle ( $\Phi = 143.2, \lambda = 1.64$ )

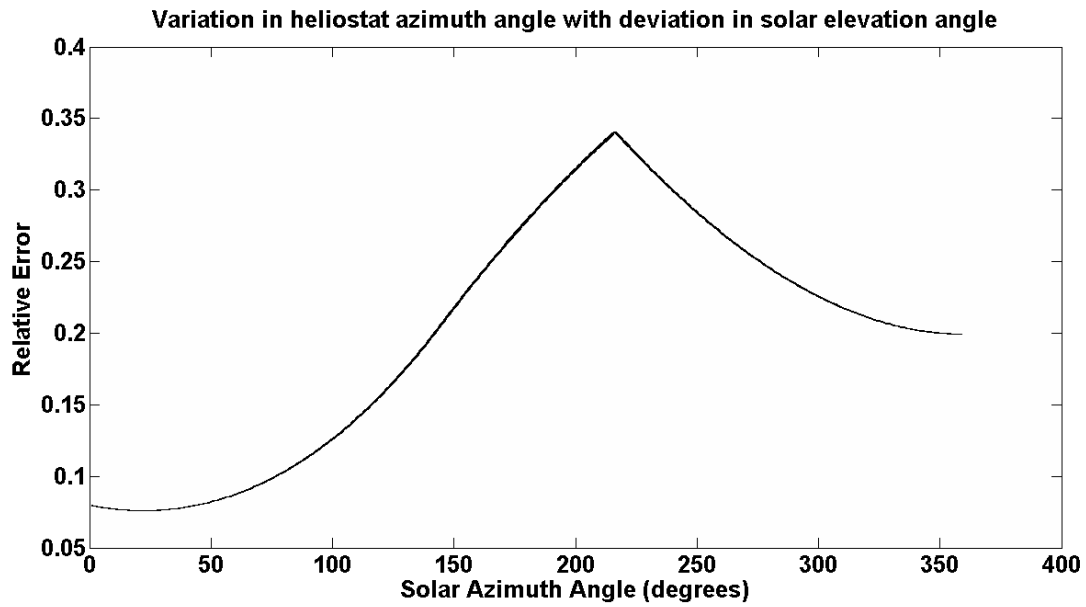


Figure 53 - Variation in heliostat azimuth positioning precision with deviation in solar elevation angle (2D- sun elevation influence is negligible). ( $\Phi = 143.2, \lambda = 1.64$ )



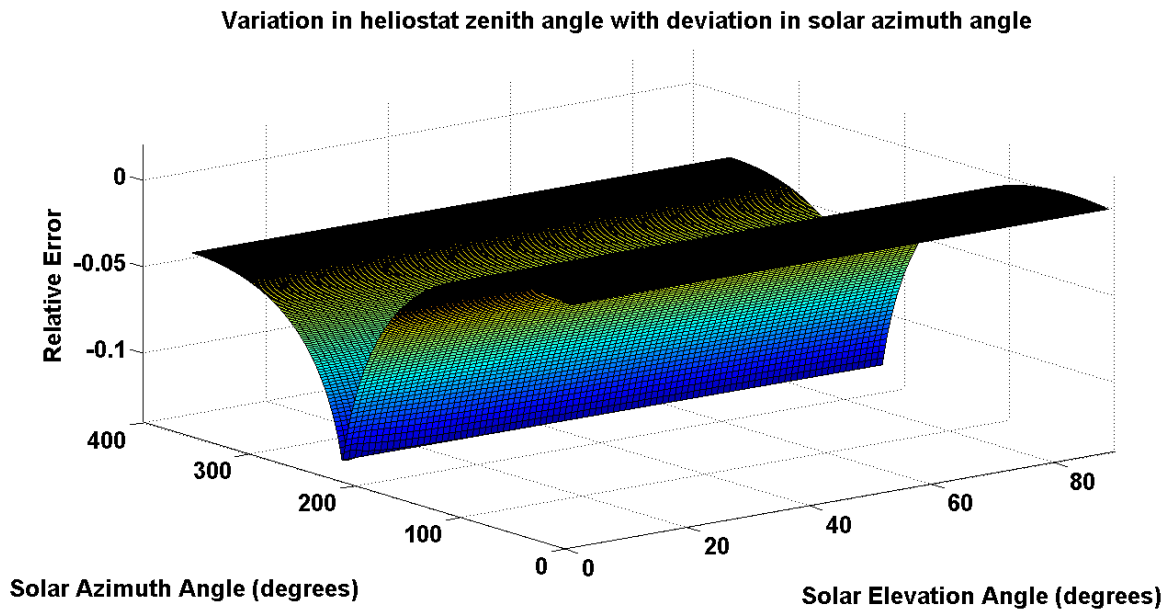


Figure 54 - Variation in heliostat elevation positioning precision with deviation in solar azimuth angle ( $\Phi = 143.2, \lambda = 1.64$ )

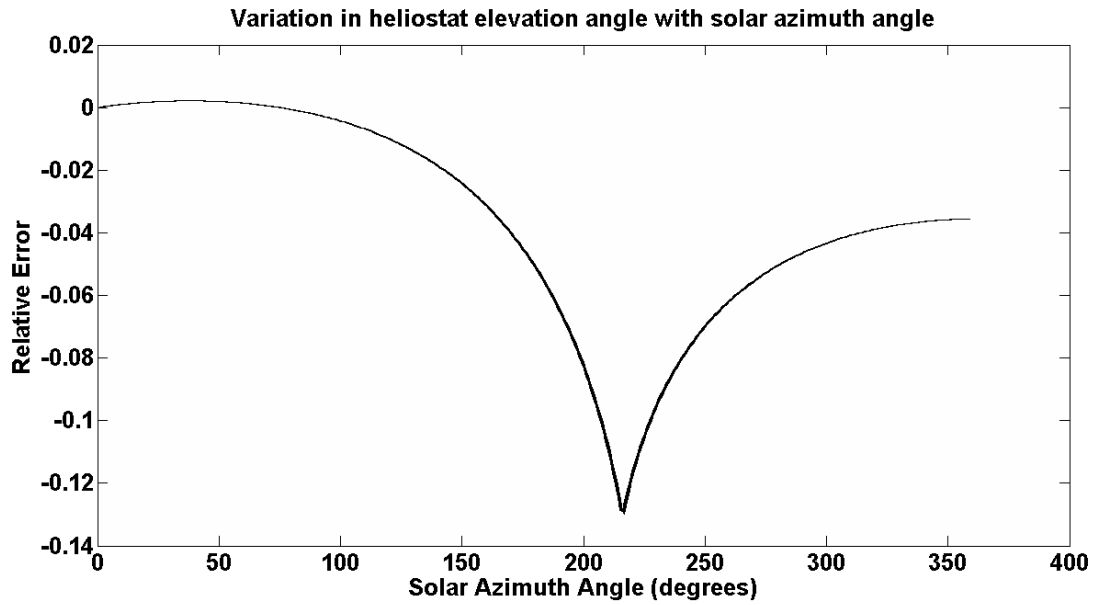


Figure 55 - Variation in heliostat elevation positioning precision with deviation in solar elevation angle (2D- sun elevation influence is negligible). ( $\Phi = 143.2, \lambda = 1.64$ )

### 9.3 ENEA – JPL

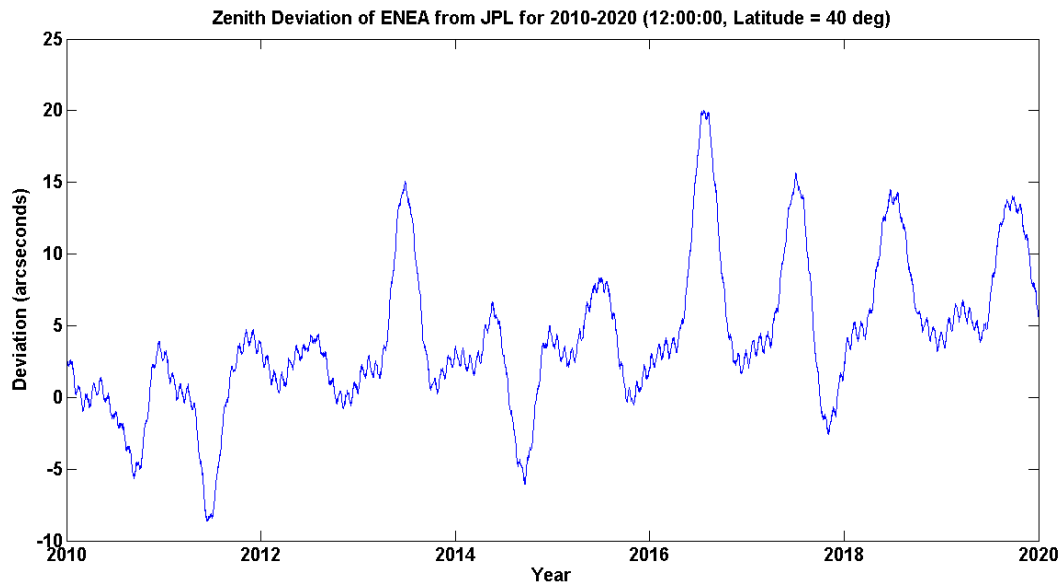


Figure 56 – Deviation of ENEA zenith with JPL zenith

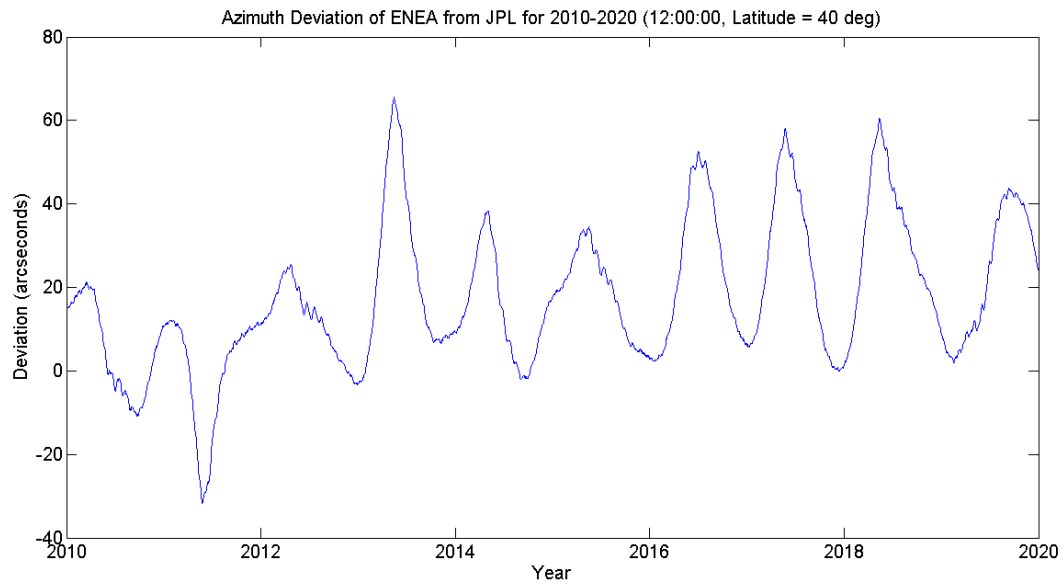


Figure 57 – Azimuth deviation of ENEA from JPL

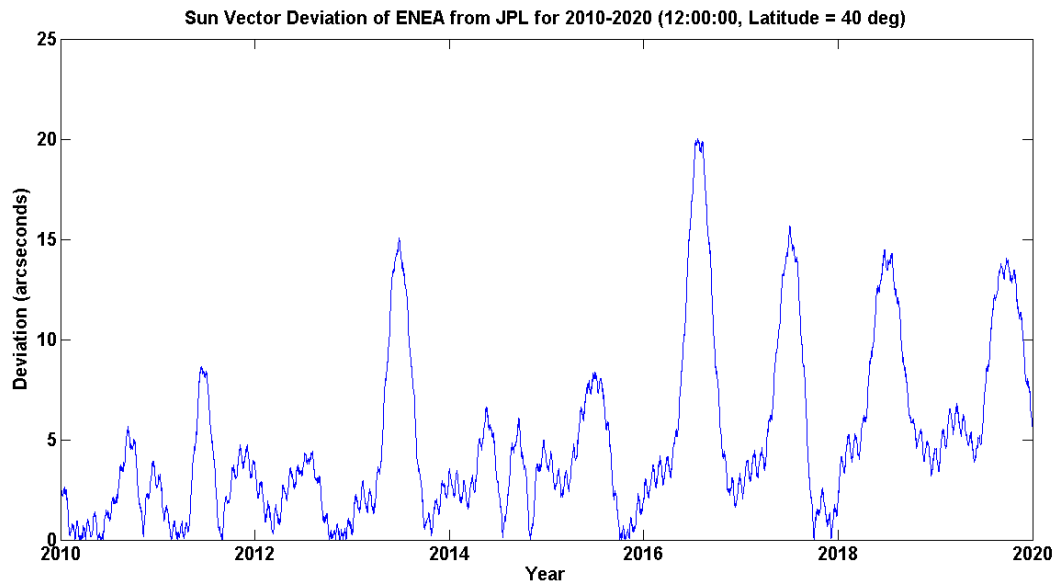


Figure 58 – Sun Vector deviation of ENEA with JPL

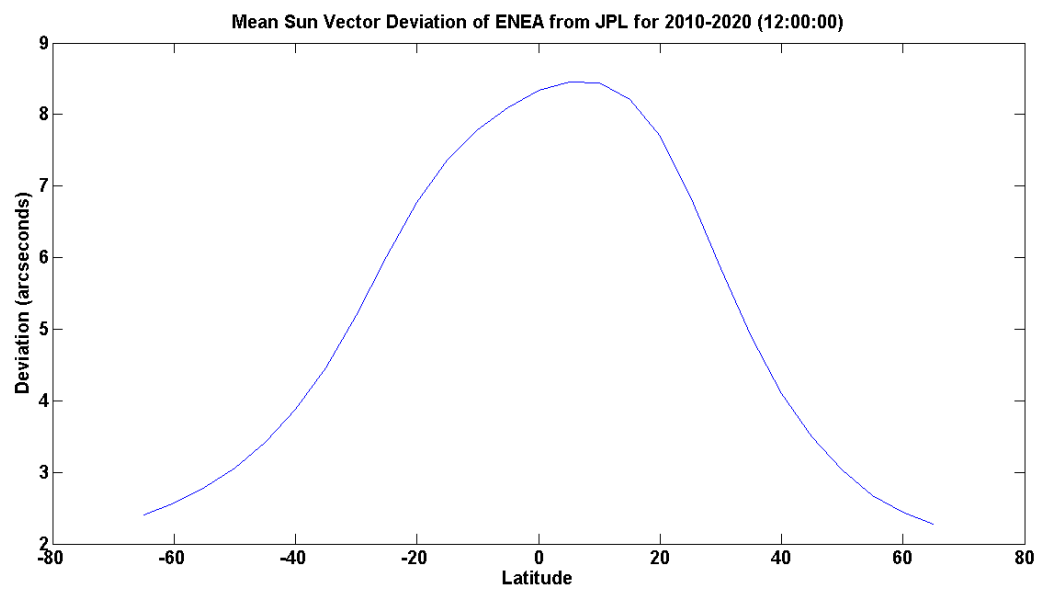


Figure 59 – Mean sun vector deviation of ENEA with JPL

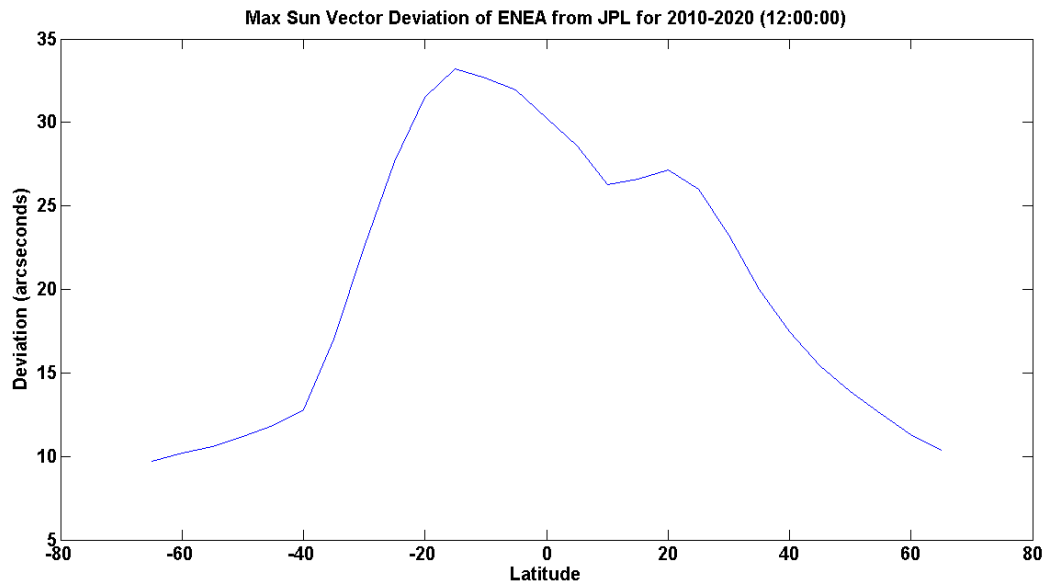


Figure 60 – Max sun vector deviation of ENEA with JPL

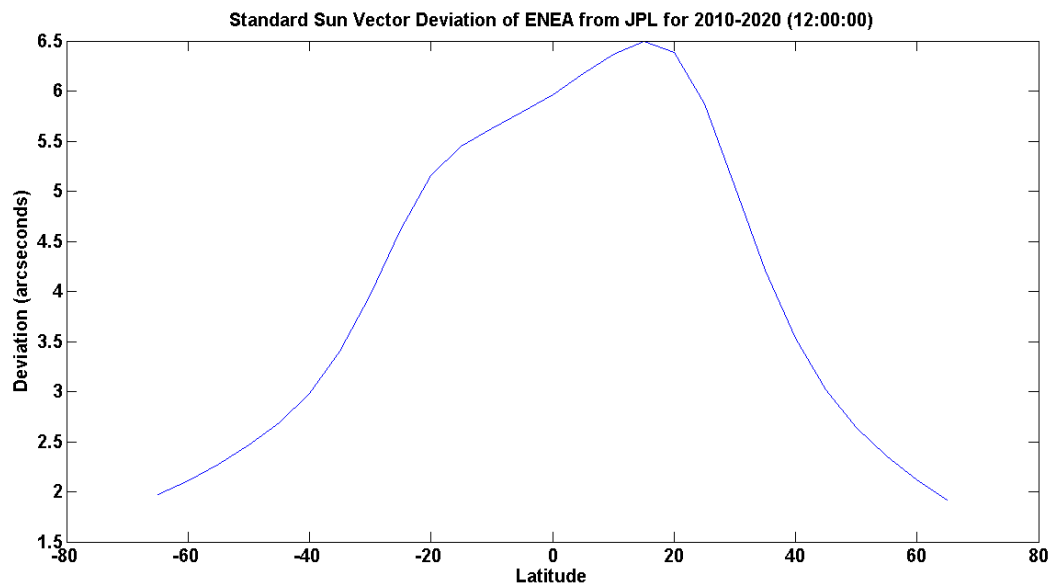


Figure 61 – Standard deviation of ENEA sun vector with JPL

## 9.4 SPA - JPL

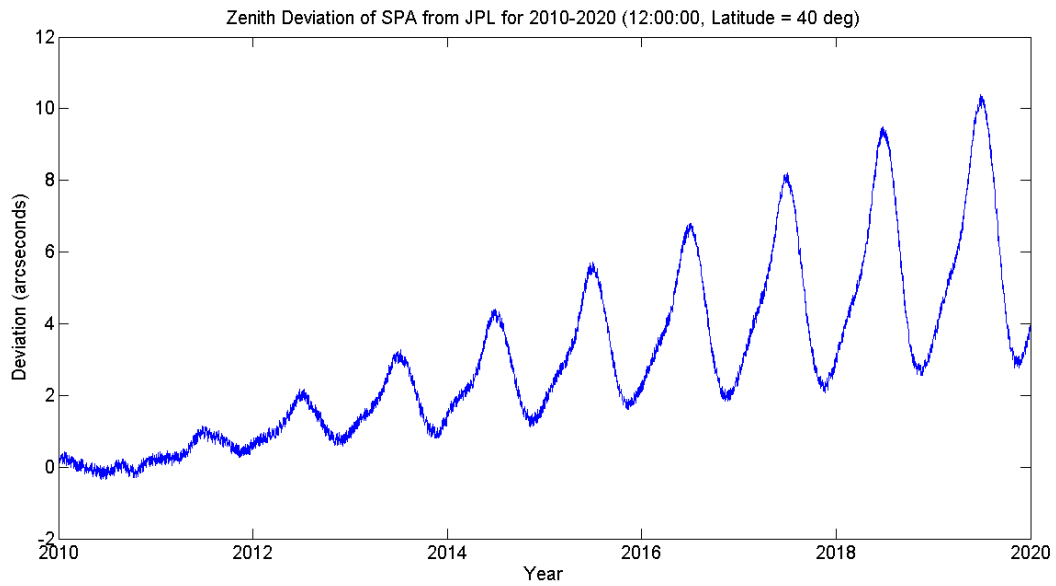


Figure 62 – Zenith deviation of SPA with JPL

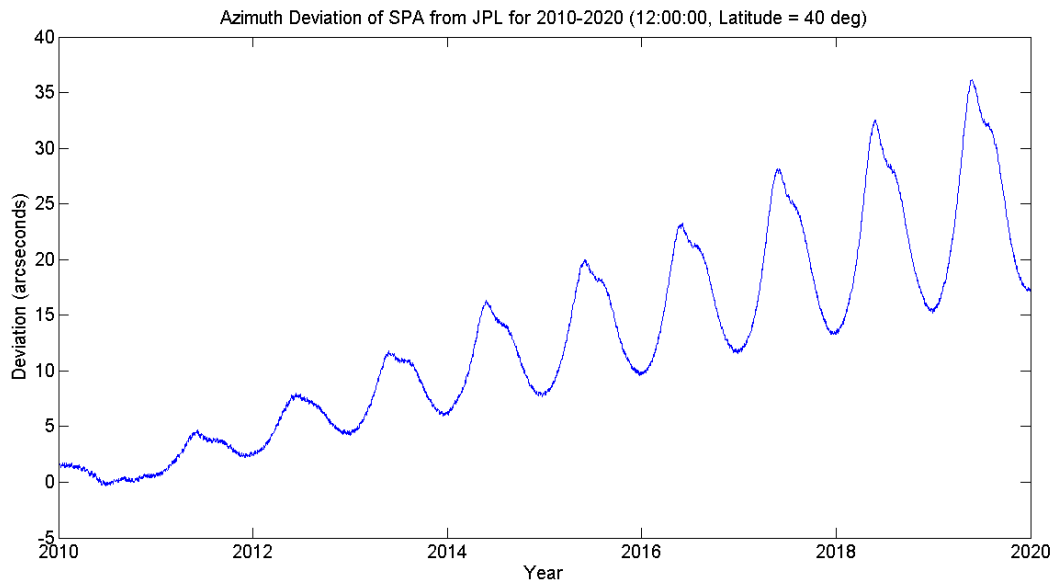


Figure 63 - Azimuth deviation of SPA with JPL

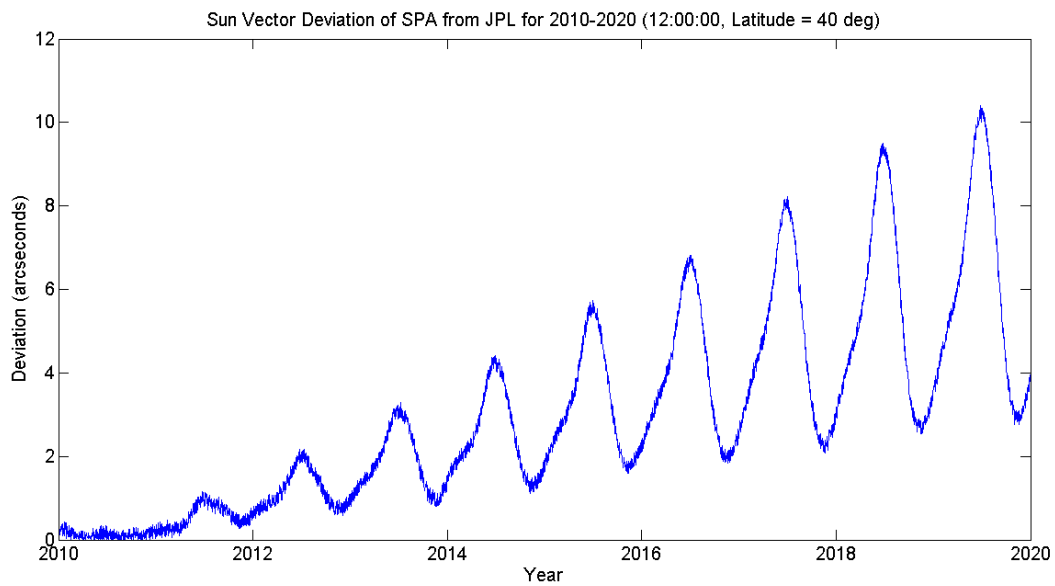


Figure 64 – Sun vector deviation of SPA with JPL

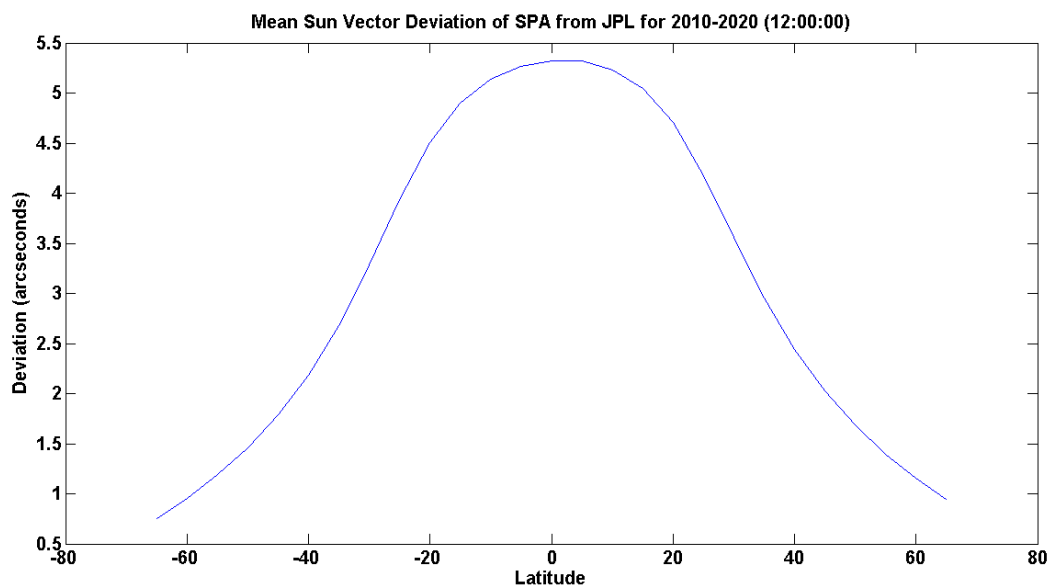
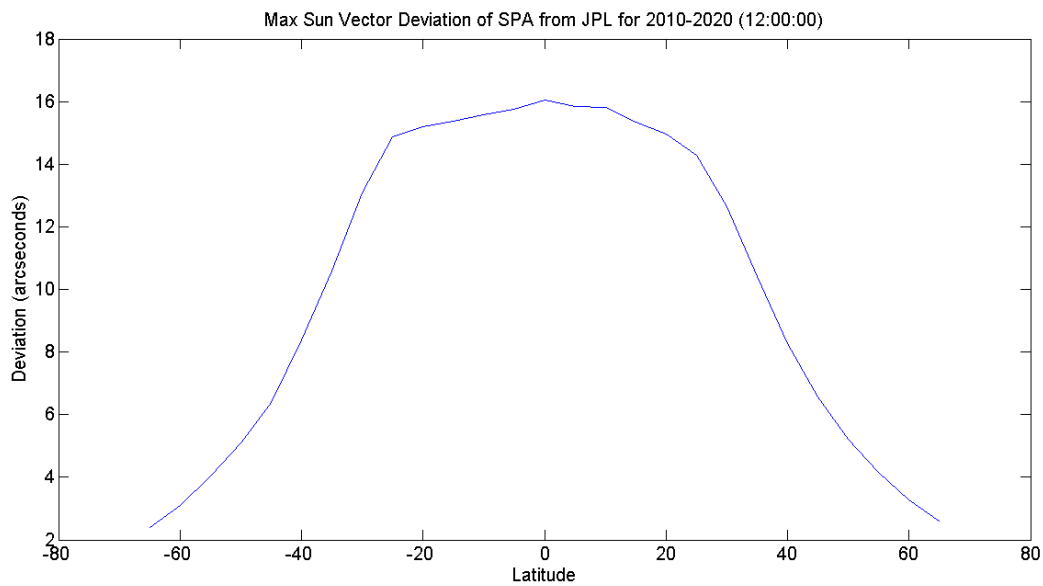
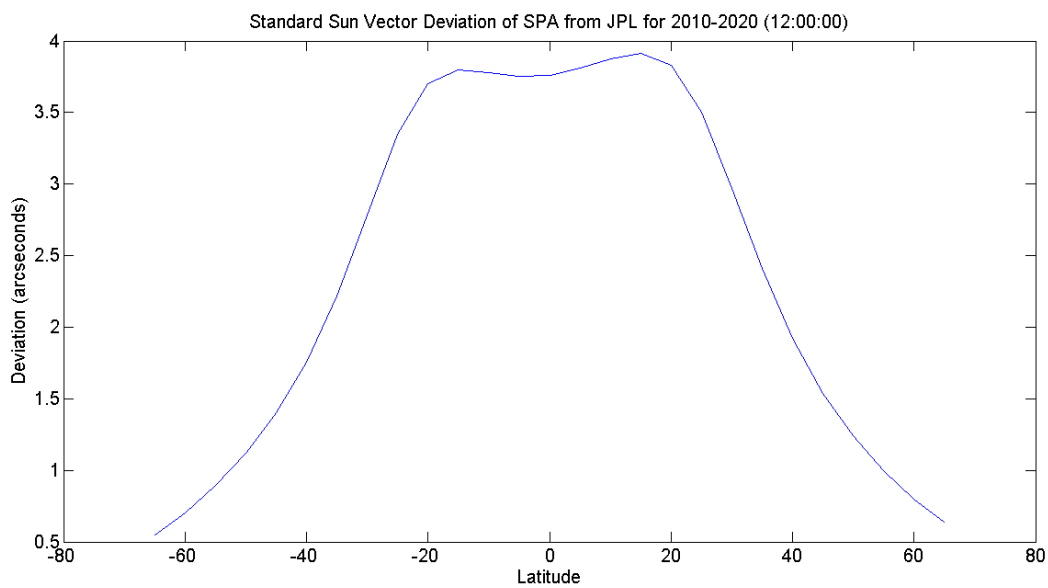


Figure 65 – Mean sun vector deviation of SPA with JPL



**Figure 66 – Max sun vector deviation of SPA with JPL**



**Figure 67 – Standard sun vector deviation of SPA with JPL**